A computational model of homeostatic cerebellar compensation of ageing in vestibulo-ocular reflex adaptation

Niceto R. Luque, Francisco Naveros, Eduardo Ros, Angelo Arleo

A computational model of homeostatic cerebellar compensation of ageing in vestibulo-ocular reflex adaptation

Niceto R. Luque [1, 2, *], Francisco Naveros[2, *], Eduardo Ros[2], Angelo Arleo[1]

[1] Sorbonne Université, INSERM, CNRS, Institut de la Vision, 17 rue Moreau, F-75012 Paris, France

[2] Department of Computer Architecture and Technology, University of Granada (CITIC), Granada, Spain

* NL and FN share the first authorship

Corresponding author: Niceto R. Luque, nluque@ugr.es

Declaration of interest: The authors hereby declare that the research was conducted in the absence of any commercial or financial relationships that could be construed as a potential conflict of interest.

Abstract

The vestibulo-ocular reflex (VOR) stabilises vision during head motion. Age-related structural changes predict a linear VOR decay, whereas epidemiological data show a non-linear temporal profile. Here, we model cerebellar-dependent VOR adaptation to link structural and functional changes throughout ageing. We posit that three neurosynaptic factors codetermine VOR ageing patterns: electrical coupling between inferior olive neurons, intrinsic plasticity at Purkinje cell synapses, and long-term spike timing dependent plasticity at parallel fibre - Purkinje cell synapses as well as mossy fibre - medial vestibular nuclei synapses. Our cross-sectional simulations show that long-term plasticity acts as a global homeostatic mechanism mediating the non-linear temporal profile of VOR. Our results also suggest that intrinsic plasticity at Purkinje cells acts as a local homeostatic mechanism sustaining VOR at old ages. Importantly, longitudinal simulations show that residual fibres coding for the peak and trough of the VOR cycle constitute a predictive hallmark of VOR ageing trajectories.

Keywords*:* vestibulo-ocular reflex (VOR), VOR ageing, cerebellar adaptation, spiking neural networks, spike timing dependent plasticity, intrinsic plasticity, electrical synapses.

1. Introduction

Healthy ageing progressively degrades postural control, balance, and spatial orientation (Anson and Jeka, 2016, Brandt et al., 2005, Zalewski, 2015). The consequent loss of static and dynamic balance hinders older adults' autonomy and it increases their risk of fall (Piirtola and Era, 2006, Desai et al., 2010, Tinetti, 2003). Postural control is an adaptive process that involves biomechanical reflexes, sensorimotor functions, as well as attentional and cognitive faculties (Horak, 2006). The sensory modalities that concurrently describe the spatiotemporal dynamics of body's position and orientation in space, include visual, vestibular, and somesthetic afferents (Lackner and DiZio, 2005, Arleo and Rondi-Reig, 2007, Cullen, 2012). The integration of these multisensory signals mediates postural control, which relies upon both body and gaze stability (Mergner and Rosemeier, 1998). Here, we focus on the vestibular control of eye movements, ensuring gaze stability during head motion (Grossman and Leigh, 1990). In particular, the vestibulo-ocular reflex (VOR) generates rapid contralateral eye movements that stabilise images on the retinal fovea during head displacements (Fig. 1A). The VOR plays a key role in maintaining balance and spatial orientation. Age-related deficits in VOR can impair visual acuity and they can lead to oscillopsia (i.e., a perturbing illusory oscillation of the visual scene) during locomotion (Demer et al., 1994).

There is evidence that healthy ageing decreases the VOR gain, i.e. the ratio between the antagonist changes of eye and head angles during head displacements (Baloh et al., 1993, Demer et al., 1994, Demer et al., 1993, Baloh et al., 2001, Agrawal et al., 2013, Li et al., 2015, Anson et al., 2016). Studies in the early 90s shed light on the impact of ageing on rotatory VOR (r-VOR) (Baloh et al., 1993, Peterka et al., 1990). A decline in the r-VOR function was observed in older adults in response to low frequency sinusoidal

rotations (<1 Hz; Peterka et al., 1990) as well as to high-amplitude and high-velocity sinusoidal rotations (Paige, 1992).Subsequent epidemiological studies reported discordant patterns of results on age-related VOR deficits, due to differences in VOR measures, tested head motion frequencies, age range, and sample size (Peterka et al., 1990, Paige, 1994, Furman and Redfern, 2001, McGarvie et al., 2015, Anson and Jeka, 2016, Li et al., 2015, Matiño-Soler et al., 2015). For instance, (Li et al., 2015) conducted a cross-sectional VOR evaluation on a study population of 110 community-dwelling adults spanning a broad age range (26-92 years, from the Baltimore Longitudinal Study of Aging cohort). They tested the VOR function by employing the video head-impulse testing (vHIT), which provides a specific clinical assessment of the peripheral vestibular system. They found is that the r-VOR gain remained stable across participants aged up to about 79-80 years, whilst it significantly declined with age afterwards (Li et al., 2015). In contrast, McGarvie et al. (2015) reported an unchanged VOR gain in older adults of 80-89 years of age, by using the vHIT for all six semi-circular canals. Similarly, Matiño-Soler et al. (2015) observed a stable r-VOR until 90 years of age and a decline afterwards. Thus, despite their discrepancies about when the VOR impairment actually occurs in older adults, all these epidemiological studies consistently found a non-linear VOR profile as a function of age, with the VOR gain remaining unchanged until 80, maximum 90 years of age, and declining thereafter. That is, the temporal dynamics of r-VOR modulation across the lifetime involve a first phase of steady, quasi linear persistence of the gain, and a second phase characterised by an abrupt drop in performances (with the cut-off occurring at 80-90 years of age).

Age-related VOR loss depends on numerous neuroanatomical properties of the vestibular system that degenerate with age (Allen et al., 2017, Anson and Jeka, 2016). The number of vestibular receptors (i.e., hair cells) decreases at a rate of about 6% per

decade, tending to degenerate from middle age on, independently from pathology (Baloh et al., 1989, Bergström, 1973). Also, the number of neurons in the vestibular nuclei undergoes a 3% loss per decade, starting at approximately 40 years of age (Alvarez et al., 2000, Lopez et al., 1996). As a consequence, throughout ageing, fewer primary vestibular afferents reach the brain, in particular the downstream control structures responsible for VOR adaptation, such as the cerebellum (Allen et al., 2017). Thus, ageing gradually hinder the detection and encoding of head displacements (in particular head rotations; Hirvonen et al., 1997). It has been suggested that neural compensatory factors (including increased sensitivity to afferent nerve fibres) may counterbalance age-related vestibular losses, thus preserving, to a certain extent, VOR in older adults (Jahn et al., 2003, Li et al., 2015, McGarvie et al., 2015). However, to the best of our knowledge, there are neither experimental nor theoretical explicit hypotheses about the compensatory mechanisms that synergistically determine the observed non-linear VOR profile across lifetime.

Here, we propose a model of cerebellar-dependent VOR adaptation to cross-link neuroanatomical and functional aspects of gaze stabilisation during head rotation. The model aimed at both reproducing epidemiological data and making testable predictions about the interplay of neuronal and plasticity mechanisms at stake during ageing. We hypothesised that three neuro-synaptic factors are critical during VOR ageing: *(i)* Electrical synaptic coupling between inferior olive neurons (through gap junctions) (Llinas et al., 1974, Sotelo et al., 1974). Electrical synapses determine the synchronicity level of the inferior olive network, thus shaping its oscillatory dynamics(Lefler et al., 2020). We considered the impact of age-related changes in the electrical coupling of inferior neurons, due to degrading GABAergic inputs from medial vestibular nuclei(Lefler et al., 2014, Best and Regehr, 2009). Because inferior olive cells are assumed to encode

retina slips during gaze stabilisation (i.e., error signalling), we evaluated to what extent age-related changes in the electrical coupling of inferior olive neurons could impact the VOR function. *(ii)* Intrinsic plasticity occurring at Purkinje cell synapses (Jang et al., 2020, Shim et al., 2018), which regulates the excitability of Purkinje neurons (by modulating their membrane capacitance) to adapt their response to synaptic morphological changes (Zhang et al., 2010, Andersen et al., 2003). We investigated the possible role of intrinsic plasticity at Purkinje cell synapses as a *local* homeostatic process, i.e., compensating for decreasing levels of vestibular afferent signals (which reach Purkinje cells through cerebellar granule cells) as well as for electro-responsiveness changes induced by ageing in Purkinje cells themselves (Zhang et al., 2010, Andersen et al., 2003). *(iii)* Long-term plasticity operating at different synaptic sites of the cerebellar circuit (Luque et al., 2019, Gao et al., 2012) Long-term potentiation (LTP) and depression (LTD) mechanisms are instrumental to cerebellar-dependent sensorimotor adaptation (D'Angelo et al., 2016). We explored their role as a *global* homeostatic compensatory process, enhancing neural sensitivity to the remaining sensory inputs during ageing.

First, we examined these tree neuro-synaptic processes independently from each other, assessing their individual impact on VOR adaptation as a function of age. Second, we simulated cross-sectional and longitudinal studies to explore how these factors may codetermine the non-linear VOR temporal pattern observed throughout ageing. Third, we sought to identify the factors responsible for the interindividual variability observed during ageing (i.e., underlying different VOR ageing trajectories across study populations). We tested the hypothesis that the variability in terms of adaptive compensation to residual fibres/connections might partially explain the apparent discrepancies between different epidemiological outcomes.

***** *Fig 1 about here* *****

134 .

135

136 # 2. Results

137 ## *Cerebellar-dependent VOR adaptation*

138 We framed cerebellar-dependent VOR adaptation within a forward control scheme (Fig.
139 1B; Lorente de Nó, 1933, Santina et al., 2001, Luque et al., 2019). Computationally,
140 the model reproduced the main properties of the cerebellar circuit, and it consisted of
141 five neural networks (Fig. 1C). A population of 100 mossy fibres (MFs) conveyed primary
142 vestibular inputs (signalling head angular accelerations) onto the cerebellar network.
143 MFs projected excitatory afferents onto both 200 medial vestibular nuclei (MVN) and
144 2000 granular cells (GCs). GCs generated a sparse representation of the MF inputs and
145 they transmitted the encoded sensory information to 200 Purkinje cells (PCs), through
146 excitatory projections. An intrinsic plasticity mechanism (Jang et al., 2020, Shim et al.,
147 2018) regulated the excitability of model PCs, consistently with electrophysiological
148 recordings (Shim et al., 2017, Turrigiano et al., 1994) (see Methods). PCs integrated the
149 afferent signals from PFs (i.e., the axons of GCs), which elicited Purkinje simple spikes
150 (i.e., tonic firing mode, see Luque et al., 2019). PCs also integrated the error-related
151 signal from climbing fibres (CFs), i.e., the axons of inferior olive (IO) cells. CFs, assumed
152 to code for retina slips, (Luque et al., 2019, Ito, 2013, Naveros et al., 2019) elicited
153 Purkinje complex spikes (i.e., bursting mode). The responses of PCs (either simple or
154 complex spiking) inhibited MVN cells, which also integrated inputs from MFs and IOs to
155 generate the cerebellar output controlling eye movements (Fig. 1C). The CF-PC-MVN
156 subcircuit comprised two symmetric microcomplexes, controlling leftward and rightward
157 eye compensatory rotations, respectively (see Methods). Long-term plasticity (LTP and

158 LTD) modulated PF-PC and MF-MVN synapses (Clopath et al., 2014, Badura et al.,
159 2016), whereas the remaining synaptic connections in the model were either non plastic
160 or electrical, as between IO cells (Fig. 1C; see Methods).

161 We assessed cerebellar-dependent r-VOR adaptation by means of a 1 Hz sinusoidal
162 head rotation protocol (i.e., within the natural head rotation range [0.05-5 Hz], Leigh and
163 Zee, 2015). During 2500 s of simulation (Fig. 2), LTP/LTD mechanisms shaped PF-PC
164 and MF-MVN synaptic efficacies (which were randomly initialised) to adapt the r-VOR
165 gain such as to reduce the error signalled by IO cells. After about 1000 s, the r-VOR gain
166 (averaged over 40 simulated individuals) plateaued at 0.95 (Fig. 2A), a value consistent
167 with experimental VOR data in humans under 1 Hz sinusoidal head rotations (Dits et al.,
168 2013). Retina slip errors, as encoded by firing of IO cells, decreased as VOR accuracy
169 improved (Fig. 2B).

170 ***** *Fig 2 about here* *****

171 ***Impact of age-related vestibular loss on the electrical coupling of Inferior***
172 ***Olive neurons***

173 Since IO neurons conveyed error-related signals mediating cerebellar sensorimotor
174 learning, we tested the impact of age-related vestibular loss on IO activity. In the model,
175 IO neurons formed an electrically coupled network, whose recurrent dynamics was
176 regulated by the PC-MVN-IO cerebellar loop (Fig. 1C). In particular, the inhibitory action
177 of MVN modulated the strength of IO electrical coupling, which in turn determined the
178 synchronicity of IO firing (Najac and Raman, 2015, Lefler et al., 2014, Best and Regehr,
179 2009). A strong IO electrical coupling (i.e., a highly synchronised IO network) would allow
180 large errors to be transmitted to PCs, eliciting fast VOR learning (Tokuda et al., 2013,

Schweighofer et al., 2013). A reduced IO electrical coupling would lead to slower but more accurate VOR adaptation (e.g., during late learning).

We sought to understand how a progressive age-related decrease of the MVN GABAergic input to IO neurons (due to vestibular primary afferent loss) would impact their network activity (Lefler et al., 2014, Best and Regehr, 2009). We simulated two age groups (20 young subjects: 20 yo; 20 older subjects: 100 yo) and we linearly decreased the inhibitory MVN input to IO as a function of age (from a maximum at 20 years to zero at 100 years, see Methods). We compared the dynamics of IO spatiotemporal firing patterns in a 5x5 lattice configuration (Nobukawa and Nishimura, 2016), when an error-related pulse activated the central IO neuron of the network (neuron 1 in Supp. Fig. 1A). The electrical coupling between IO neurons produced a rapid transient propagation within the network, eliciting a sequential bursting of IO cells along the radial outward direction of the lattice (Supp. Figs. 1A, B). When comparing IO network propagation patterns across age, we found that the central stimulation did elicit more rapid and pronounced membrane potential variations in the IO lattices of older individuals, which resulted in simpler on/off network dynamics as compared to young individuals (Fig. 3A and Supp. Figs. 1B, C). Also, this transient on/off patterns produced a higher mean activation frequency in older IO networks (Fig. 3A). We quantified the complexity of IO spatiotemporal patterns by using the Discrete Wavelet Transform (DWT) (Latorre et al., 2013). DWT considered these patterns as sequences of images (obtained every ms) and it estimated the compression rate of each image by calculating the DWT coefficients. High (low) DWT values corresponded to complex (simple) spatial structures of IO network patterns at a given time. We found that the electrical coupling among IO neurons in older individuals gave rise to significantly simpler spatiotemporal network activations, as compared to young individuals (Fig. 3B; ANOVA $F_{(294,16)}=18$, $p < 10^{-7}$). This was

206 consistent with a more uniform and synchronised activity of older IO neurons, and with
207 a higher mean frequency (Fig. 3A). The simpler spatiotemporal dynamics of older IO
208 networks were likely to induce a poorer capacity to encode retina slips. Therefore, we
209 subsequently tested the impact of this less effective error signalling on VOR
210 performance.

211 ***** Fig 3 about here *****

212 ## *Impact of age-related vestibular loss on r-VOR performance*

213 First, we investigated the consequences of age-related vestibular degradations on the
214 VOR function without any compensatory mechanism in the downstream cerebellar
215 network. To do so, we blocked intrinsic plasticity at PC synapses as well as LTP/LTD at
216 MF-MVN and PF-PC synapses. We simulated a cross-sectional study over a large-scale
217 study population of 2400 individuals aged from 40 to 100 years, by taking a group of 40
218 individuals per each of year of age (i.e., uniform distribution). Each individual underwent
219 an independent 1 Hz head rotation protocol (during 2500 s, as above). At the beginning
220 of the ageing simulation, the cerebellar synaptic weights of each 40-year-old individual
221 were those obtained at the end of r-VOR learning (Fig. 2). Then, a loss of primary
222 vestibular afferents took place as a function of age, based on a degeneration rate of 3%
223 MVN neurons per decade (Lopez et al., 1996, Alvarez et al., 2000). The loss of MVN
224 neurons induced a change in the MVN-IO inhibitory action, which in turn gradually
225 increased the electrical coupling within the IO network (Najac and Raman, 2015, Lefler
226 et al., 2014, Best and Regehr, 2009). The age-related degradation of vestibular primary
227 afferents also translated into a loss of 0.3% MF-MVN connections per year, as well as
228 0.3% MF-GC projections per year (starting at 40 yo). In addition, the simulated ageing
229 accounted for a loss of approximately 6% of GCs per decade (Baloh et al., 1993,

Bergström, 1973, Renovell et al., 2001, Viswasom et al., 2013), which engendered a degradation of 0.6% of PF-PC connections per year. Each of the 2400 individuals independently lost a number of *randomly selected* fibres and neurons as a function of age, based on the above degeneration rates.The results of the ageing simulation showed a steady decline of the VOR function (Figs. 3C-E), with the accuracy of the r-VOR gain significantly impaired. Across the study population, the VOR gain declined quasi-linearly as a function of age (Fig. 3E), in contrast to actual epidemiological data (e.g., Li et al., 2015).

Intrinsic plasticity at Purkinje cell synapses as a local homeostatic mechanism

The detailed Purkinje cell (PC) model reproduced the three characteristics spiking patterns observed experimentally (Fig. 4A): simple spiking response (i.e., tonic firing at 10-250 Hz), complex spiking response (i.e., bursting activity up to 600 Hz), and post-complex spike pauses. We previously showed that Purkinje spike burst-pause dynamics are likely to play a key role in VOR adaptation and reversal learning (Luque et al., 2019). Here, we investigated the consequences of age-dependent changes of PC excitability on the VOR function. With ageing, the number and the surface of PC synapses decrease significantly (Zhang et al., 2010). We reasoned that intrinsic plasticity could adapt the response of PCs during ageing (thus acting as a local homeostatic mechanism). The membrane capacitance of model PCs decreased as a function of age (Li and Li, 2013) (Fig. 4B; see Methods). This led to an increase of tonic firing rates in older PCs (Fig. 4C), consistently with electrophysiological data (Zhang et al., 2010). We also assessed the relation between the duration of post-complex spike pauses and the duration of pre-complex spike ISIs in model PCs. We realised this measure by incrementally increasing the PF inputs whilst maintaining the CF stimulation constant (i.e., only ISIs immediately

following complex spikes were considered for this analysis, as in experimental data, Grasselli et al., 2016). The PC model with the intrinsic plasticity mechanism predicted that the linear relation between the duration of post-complex spike pauses and the duration of pre-complex spike ISIs would be preserved during ageing (Fig. 4D; R^2 = 0.9932; $p < 10^{-4}$).

We then ran a second ageing simulation to test to what extent PC intrinsic plasticity may operate in the presence of vestibular loss. We mimicked again a cross-sectional study by taking a sample of 2400 individuals (age range: 40-100 yo; 40 individuals per each year of age). Each individual underwent the same VOR adaptation protocol (1 Hz sinusoidal rotation during 2500 s). The initial conditions (in terms of cerebellar synaptic weights) corresponded to those obtained after r-VOR learning per each independent individual (Fig. 2A). Age-dependent vestibular (and MVN) degeneration translated into a loss of 0.3% and 0.6% MFs and PFs per year, respectively. As a consequence of MVN loss, the IO electrical coupling progressively increased with age (Najac and Raman, 2015, Lefler et al., 2014, Best and Regehr, 2009). All LTP/LTD mechanisms at MF-MVN and PF-PC synapses were blocked, such as to isolate the effect of the local homeostatic mechanism provided by intrinsic plasticity at PCs. We found that the increasing excitability of PCs could partially counterbalance the decreased depolarising currents elicited by PFs throughout ageing. This resulted in a quasi-linear decrease of the r-VOR gain across lifetime, along with an increasing interindividual variability (Fig. 4E)

***** *Fig 4 about here* *****

Cerebellar spike-timing dependent plasticity as a global homeostatic compensatory mechanism

Spike-based plasticity mediated LTP/LTD at PF-PC and MF-MVN synapses during r-VOR learning (Fig. 2). We tested whether this adaptation mechanism could enhance the sensitivity of PCs and MVN to degraded input signals during ageing. First, we analysed the weight distributions at PF-PC and MF-MVN synapses after r-VOR learning as a function of age. We compared the synaptic weights of simulated young and older individuals (20 and 100 yo, respectively). In both age groups, cerebellar learning led to anti-symmetric weight distributions at both PF-PC and MF-MVN synapses (Fig. 5), corresponding to the two microcomplexes that controlled rightward and leftward eye movements. Expectedly, the inhibitory action of PCs onto MVN generated opposite weight patterns at PF-PC as compared to MF-MVN synapses (Figs. 5A, B *vs*. 5C, D). In older individuals, an increase of the weights of the remaining fibres compensated the loss of vestibular afferents (Figs. 5B, D). When comparing the distributions obtained by the normalised sums of synaptic weights across PFs (i.e., to estimate the input drive received by PCs), we found platykurtic-like distributions in older individuals (Figs. 5B,D) as compared to more leptokurtic profiles in young individuals (Figs. 5A,C). The ratio between the number of saturated synaptic weights and the number of active afferents increased significantly with age: 28% in young vs. 64% in older PF-PC synapses (Fig. 5A vs. 5B); and 21% in young vs. 31% in older MF-MVN synapses (Fig. 5C vs 5D). Consequently, the neural drive (defined as the area obtained by convolving a unitary impulse signal with the weight distributions) increased significantly with age: it was 2.64 times larger in the older PF-PC synaptic distribution, and 1.64 times larger in the older MF-MVN synaptic distribution, as compared to younger individuals, respectively.

***** *Fig 5 about here* *****

We then ran a third cross-sectional ageing simulation to isolate the role of spike-based cerebellar LTP/LTD in preserving VOR accuracy across lifetime (i.e., by blocking intrinsic plasticity at PC synapses). Again, we considered a study population of 2400 individuals (age range: 40-100 years; 40 individuals per each year of age) and we applied the same VOR protocol (1 Hz head rotation during 2500 s). We found that compensatory LTP/LTD at PF-PC synapses increased the input drive to PCs from 40 to 60 years (Fig. 6A). However, from 60 to 75 years, increasing the neural sensitivity of PCs only could not maintain the same level of neural drive. Thus, a rapid boost of neural sensitivity at MVN synapses sustained the neural drive (Fig. 6B). Beyond 80 years of age, the neural inputs driving both PC and MVN responses could no longer be maintained against age-related vestibular losses (Figs. 6A,B), which impaired the learning of sensorimotor associations underpinning VOR accuracy. Accordingly, the r-VOR gain remained unchanged until about 80 years and it declined significantly afterwards, accompanied by higher performance variations across individuals (Fig. 6C).

***** *Fig 6 about here* *****

Impact of ageing on the VOR function: cross-sectional and longitudinal analyses

We combined all age-related factors and all compensatory mechanisms examined so far to assess their synergistic impact on r-VOR adaptation. First, we ran a fourth cross-sectional ageing simulation by taking again a study population of 2400 individuals (age range: 40 - 100 yo), with each individual undertaking the same r-VOR adaptation protocol (1 Hz sinusoidal head rotation during 2500 s). Intrinsic plasticity at PC synapses and LTP/LTD at MF-MVN and PF-PC synapses provided local and global homeostatic adaptation, respectively, to age-related alterations. Simulation results suggested that the

above factors interacted to shape the r-VOR function across the lifespan. In agreement with cross-sectional analyses in humans, the r-VOR performances remained quasi-stable until 85-90 years of age, after which it declined sharply at a rate of 0.8% per year (Fig. 7A). The contribution of PCs' intrinsic plasticity allowed the VOR function to be sustained further in age as compared to when only LTP/LTD adaptation was present (Fig. 7B). The variability across individuals increased smoothly until 80 years and it then augmented significantly (up to 4 times larger at 100 years of age, Fig. 7C), consistently with the tendency observed experimentally (e.g., Li et al., 2015).

***** *Fig 7 about here* *****

Second, we ran a longitudinal ageing simulation. We took a study population of 40 individuals and we emulated a 60-year follow-up for each of them (i.e., from 40 to 100 yo). Again, we considered a loss of 0.3% and 0.6% of MFs and PFs loss per year, respectively. Also, age-related changes of MVN GABAergic inputs to IO shaped the electrical coupling within the IO network as before. However, in contrast to the previous cross-sectional scenario, these neural losses accumulated across the lifetime of each individual. Expectedly, the VOR performance across the study population remained quasi-stable until about 85 yo and it declined sharply afterwards (Fig. 7D). The interindividual variability increased significantly during the last 15 years of age and it became almost 5 times larger at 100 yo as compared to 85 yo (Fig. 7C).

Finally, we sought to understand the underlying factors determining the difference between steady and declining VOR trajectories (e.g., thick green curve vs. thick red curve in Fig. 7D, respectively). Knowing that: *(i)* all individuals of same age had the same probability of losing vestibular primary afferents, MVN, MFs, and PFs; *(ii)* the degeneration process affected fibres and neurons based on a random selection; *(iii)* the

local and global homeostatic mechanisms (i.e., intrinsic plasticity and LTP/LTD) operated equally across all individuals, we reasoned that a possible determinant of the VOR ageing trajectory could lie in the distribution of the remaining (i.e., post age-related loss) fibres/synaptic connections. We postulated that the activity of some subsets of the remaining connections may be more critical than others in terms of information content for the encoding of sensorimotor associations and then to maintain the VOR function. To test this hypothesis, we first sorted all individuals on the basis of their VOR gain performance at 100 years (Fig. 8A; the red and green dots corresponded to the worst and best aging trajectories of Fig. 7D, respectively). Then, we compared the subsets of residual connections that were active at specific moments of the VOR cycle across individuals. We found that the number of remaining connections responsible for the encoding of the peak and the trough of the eye velocity function (Fig. 8B) correlated significantly with the VOR performances of 100-year-old individuals (Fig. 8C, right column; Supp. Fig. S2). That is, the sorting of 100yo individuals based on their residual VOR performance matched perfectly the sorting of the same individuals based on the number of residual PFs and MF-MVN projections coding for the sinusoid's peak and trough (Fig. 8C, right column). Strikingly, this strong correlation held already at 85 years of age (i.e., the cut-off age between steady and declining VOR trajectories; Fig. 8C, centre) and even much earlier, at 60 years of age (i.e., numerous years before the discontinuity time point between "good" and "bad" ageing trajectories; Fig. 8C, left). Given that the overall number of lost connections was the same across all the study population, this implied that those individuals that *by chance* had most of the remaining connections involved in the encoding of those two critical moments in the VOR period (i.e., between 200-300 ms and 700-800 ms) had the best chances to have stable VOR performances throughout ageing.

***** *Fig 8 about here* *****

3. Discussion

We modelled cerebellar-dependent sensorimotor adaptation to study how ageing alters the VOR function. The spiking neural model captured the main computations made by the cerebellum and it reproduced the biophysical properties of PCs, which are core to sensorimotor learning. The model offered a transparent tool to assess the impact of age-related vestibular losses on downstream, cerebellar adaptive coding of gaze stability (during head rotations). The proposed model complements previous qualitative VOR models that addressed age-related issues (Anson et al., 2016, Baloh et al., 1993, Li et al., 2015, Paige, 1992, Peterka et al., 1990) by providing a more mechanistic insight into the factors underpinning VOR ageing. We hypothesised that three neurosynaptic factors are key to the understanding of the link between age-related anatomical and functional VOR changes: the electrical coupling between inferior olive neurons, the intrinsic plasticity at PC synapses, and LTP/LTD at PF - PC as well as MF - MVN synapses.

To test this hypothesis, we ran a series of ageing simulations to single out the role of these three factors in determining VOR changes throughout ageing. First, we found that age-related vestibular loss caused the spatiotemporal patterns of the IO network to become simpler, similar to an on/off ensemble dynamics. This reduced the accuracy of retina slip (i.e., error) coding, which in turn impaired VOR adaptation. As a consequence, our first cross-sectional ageing simulation (which isolated the effect of vestibular loss and IO coupling alteration, with no compensatory mechanism in the downstream cerebellar network) showed a linear VOR decline as a function of age (i.e., following the steady vestibular degeneration). This result contrasted epidemiological data in humans, which rather show a non-linear VOR temporal profile (with VOR remaining stable until 85-90

398 years of age and declining abruptly afterwards, Li et al., 2015, Matiño-Soler et al., 2015,
399 McGarvie et al., 2015). Second, we assessed the local homeostatic action provided by
400 PC intrinsic plasticity, which adaptively increased PC excitability throughout ageing
401 (countering the decreasing levels of PF afferents, due to the loss of vestibular signals
402 integrated by cerebellar granule cells). At the level of single PCs, the tonic firing rates
403 increased with age according to experimental data (Zhang et al., 2010), whereas the
404 linear relation between the duration of post-complex spike pauses and the duration of
405 pre-complex spike ISIs did not change during ageing (testable prediction). At the level of
406 the VOR function, our second cross-sectional simulation (which accounted for age-
407 related vestibular loss, IO coupling changes, and PC intrinsic plasticity) showed that the
408 adaptively increasing excitability of PCs could only moderately counter the impaired
409 encoding of sensory (vestibular) - motor (eye movement) associations, resulting in a
410 linear decline in VOR accuracy over the years (again, in contrast with actual
411 epidemiological data). Third, we isolated the impact of LTP/LTD at PF - PC and MF -
412 MVN connections and we quantified the increase of synaptic weights to adapt the neural
413 drive of PCs and MVN to degrading input signals. The results from another cross-
414 sectional ageing simulation (accounting for age-related vestibular loss, IO coupling
415 changes, and LTP/LTD) captured the two regimes of human VOR performances during
416 ageing. That is, LTP/LTD sustained the sensorimotor associations underlying the VOR
417 function by enhancing the neural sensitivity to residual afferent signals throughout ageing
418 (i.e., it allowed the full synaptic range to be exploited in order to maintain constant the
419 neuronal drives). However, the compensatory action by LTP/LTD became ineffective in
420 the presence of significant levels of vestibular losses (i.e., beyond 80 yo), because
421 synaptic weights saturated in PF-PC and MV-MVN connections.

We ran a fourth cross-sectional simulation to assess how the three neuro-synaptic factors would concurrently work during VOR adaptation. The results confirmed that the global homeostatic compensation mediated by cerebellar LTP/LTD was primarily responsible for the non-linear temporal profile observed in VOR epidemiological data (e.g., Li et al., 2015). This prediction is consistent with the saturation hypothesis by (Nguyen-Vu et al., 2017), stating that an intense change of the synaptic strength shall temporarily prevent further adaptation. They showed that a specific type of pre-training that desaturates synapses can improve the ability of mutant mice to learn an eye-movement task. Conversely, they found that a specific procedure that saturates synapses can impair the learning ability. In our model, the progressive saturation of PF-PC and MF-MVN synapses limited VOR adaptation, thus impairing the compensatory action of LTP/LTD in oldest individuals and leading to the non-linear VOR dynamics throughout ageing. Our results also showed that the local homeostasis implemented by intrinsic plasticity at PC synapses played a role in further sustaining VOR between 80 and 90 years of age and in attenuating its decline rate afterwards. A compensatory action related to intrinsic plasticity at PCs was recently reported during long-term VOR consolidation in mice (Jang et al., 2020). Interestingly, the slope attenuation due to intrinsic plasticity while compensating VOR decline in the model was within the same range as that observed in mice (Jang et al., 2020).

Finally, we further exploited the model vantage point to run a longitudinal ageing simulation. This allowed us to follow individual ageing trajectories over 60 years, in the attempt to better understand the factors determining interindividual differences across ageing (i.e., differentiating steady vs. declining VOR trajectories). Strikingly, we found that the number of remaining PFs and MF-MVN projections coding for the peak and the trough of the VOR cycle provided a predictive hallmark for the VOR ageing trajectory on

a single-subject basis. That is, those individuals lacking active PF and MF-MVN afferents in those precise moments could robustly be expected to have more difficulties in VOR adaptation throughout ageing. This prediction could possibly be tested in animal models by seeking for those fibres that are most active when the ocular velocity is maximal during VOR. For instance, the identification of specific cerebellar GCs (and of their PFs) that are active upon induction of specific stimulation is possible in vivo mice experiments (Ishikawa et al., 2015).

The model presented here assumed that the GC layer univocally encoded vestibular (head motion related) signals through the temporal activation of non-overlapping cell populations during cerebellar VOR adaptation. GCs are thought to encode vestibular signals into sparse representations allowing interferences across tasks to be minimised and neuronal resources to be optimised by reducing redundancy (D'Angelo and De Zeeuw, 2009). The recurrent inhibitory Golgi cells - GC connections suggest that the granular layer may act as a recurrent dynamic network (Yamazaki and Tanaka, 2005) Thus, GCs are likely to generate a randomly repetitive network response characterised by active/inactive state transitions with no repetition of active cell populations (Yamazaki and Tanaka, 2007). The model also assumed a progressive degradation of vestibular afferents integrated by the GC layer with ageing (Baloh et al., 1989, Bergström, 1973), which led to a degradation of PFs, impairing, in turn, long-term PF-PC synaptic adaptation. Interestingly, neural regeneration can occur at PF-PC synapses thanks to the Gluδ2 receptor (Ichikawa et al., 2016), whereas Gluδ2 deficits lead to disruption of LTD at PC synapses and motor impairment in VOR tasks (Pernice et al., 2019, Yuzaki, 2013). Some evidence suggests that neural loss can be related to the absence of Gluδ2 receptor, since the deletion of GluRδ2 expression in mutant mice (GluRδ2ho/ho) induces PC and GC reduction over lifetime (Zanjani et al., 2016). A gradual decrease on Gluδ2

with ageing would compromise Gluδ2-dependent processes that, in turn, would reduce intrinsic PC excitability and eventually impair LTD at PCs.

The model also assumed a compromised IO electrical coupling due to degraded GABAergic afferents from MVN during ageing. The strength of the gap junctions amongst modelled olivary neurons was asymmetric (Lefler et al., 2014, De Zeeuw et al., 1998). The level and the direction of this asymmetry was regulated by emulating the GABAergic feedback (Lefler et al., 2014). The coupling asymmetry allowed for the creation of different spatial configurations of PC's complex spike patterns. The GABAergic inputs from MVN could directly cause a transient decrement in electrical coupling amongst IO cells (Lefler et al., 2014). GABAergic feedback not only temporarily blocked the transmission of signals through the olivary system but it could also isolate IO neurons from the network by shunting the junction current (Loewenstein, 2002). In the absence of GABAergic feedback, electrical coupling was not counteracted and IO network oscillations were not mitigated but rather increased. There is only indirect evidence for an age-related degeneration of the GABAergic MVN inputs throughout aging. The r–aminobutyric acid, GABA, inhibits the formation of lipoxidation end products (Deng et al., 2010). The presence and accumulation of lipofuscin with ageing, a lipoxidation product, is an essential part of the traditional theory of ageing (Sulzer et al., 2008). Lipofuscin accumulates in postmitotic cells with age, impairing their functioning. Its presence is caused by unbalanced cell metabolic and waste-degradation functions. IO neurons are relatively immune to apoptosis (Lasn et al., 2001) and they preserve their function with ageing, although they tend to accumulate significant amount of lipofuscin with age (Brizzee et al., 1975). It is unclear whether the presence of a large amount of lipofuscin is due to higher lipofuscin generation and/or decelerated removal (Fonseca et al., 2005). Since lipofuscin aggregates are unavoidable reactions in biological systems,

497 the lack of a cycle involving lipofuscin elimination is more plausible than the absence of
498 lipofuscin generation (Yin, 1996). The r-aminobutyric acid scavenging effects proposed
499 by Deng et al. (2010) over advanced lipoxidation end products (ALEs) may be
500 instrumental for lipofuscin clearance in the olivary system. A gradual decline of r–
501 aminobutyric acid presence with age, may explain the accumulation of lipoxidation
502 products in IO neurons. MVN GABAergic afferents are the main source of r–aminobutyric
503 acid for the olivary cells but they also mediate the electrical coupling amongst them. The
504 gradual degeneration of these GABAergic afferents may explain the gradual presence
505 of IO lipofuscin as well as the altered activations of IO ensembles with ageing.

506 # 4. Methods

507 ## *Vestibulo-Ocular Reflex (VOR) Model*

508 The VOR was defined as a continuous-time mathematical model with two poles (Eq. 1),
509 whose parameters were adjusted recursively to fit experimental and clinical data
510 (Skavenski and Robinson, 1973, Robinson, 1981, Gordon et al., 1989):

511 $$VOR(s) = \frac{E(s)}{H(s)} = \frac{K \cdot T_{c1} \cdot s}{(T_{c1} \cdot s + 1) \cdot (T_{c2} \cdot s + 1)} \cdot e^{-s\tau_{delay}} \quad (1)$$

512 Where $e(t), E(s): eye\ motion\ (output)$, and $h(t), H(s): head\ motion\ (input)$.

513 There were 4 parameters in the model: $Q = [K, T_{C1}, T_{C2}, \tau_{delay}]$. The delay parameter
514 τ_{delay} captured the delay in communicating the signals from the inner ear to the brain and
515 the eyes. This delay is the consequence of the time needed for neurotransmitters to
516 traverse the synaptic clefts between nerve cells. Based on the number of synapses
517 involved in the VOR, the estimate of this delay is of 5 ms (Skavenski and Robinson,

1973, Robinson, 1981). The gain parameter *K,* assumed to be between 0.6 and 1, modelled the fact that the eyes do not perfectly cope with the movement of the head(Skavenski and Robinson, 1973, Robinson, 1981). The T_{c1} parameter represented the dynamics associated with the semicircular canals as well as some additional neural processing. The canals are high-pass filters, as the neural active membranes in the canals slowly relax back to their resting position after rotational experimentation (the canals stop sensing motion). Based on the mechanical characteristics of the canals, combined with additional neural processing which prolongs this time constant to improve the VOR accuracy, the T_{c1} parameter was estimated to be around 15 sec, in agreement with the biologically range which is 10-30 sec (Skavenski and Robinson, 1973, Robinson, 1981). Finally, the T_{c2} parameter captured the dynamics of the oculomotor plant, i.e. the eye and the muscles and tissues attached to it. Its value was between 0.005 and 0.05 sec.

To find the temporal response for the VOR transfer function, we needed to calculate the inverse Laplace transform (Eq. 2). The outcome of the inverse Laplace transform consisted in a differential equation system defined in the same time domain as the spiking cerebellar network (see below; note that we modelled the delay and we inserted within the sensorimotor delay).

$$\begin{bmatrix} \dot{x}_1 \\ \dot{x}_2 \end{bmatrix} = \begin{bmatrix} 0 & 1 \\ -a_0 & -a_1 \end{bmatrix} \cdot \begin{bmatrix} x_1 \\ x_2 \end{bmatrix} + \begin{bmatrix} 0 \\ h(t) \end{bmatrix}$$
$$e(t) = \begin{bmatrix} b_0 & b_1 \end{bmatrix} \cdot \begin{bmatrix} x_1 \\ x_2 \end{bmatrix} \quad (2)$$

Where:

538
$$a_0 = \frac{1}{T_{c1} \cdot T_{c2}}, \quad a_1 = \frac{T_{c1} + T_{c2}}{T_{c1} \cdot T_{c2}}$$
$$b_0 = 0, \qquad b_1 = \frac{K \cdot T_{c1}}{T_{c1} \cdot T_{c2}}$$

539 *VOR analysis and assessment.* The periodic functions representing eye and head
540 velocities were analysed through a discrete-time Fourier transform:

541
$$FFT\,X(k) = \frac{1}{N}\sum_{n=0}^{N-1} x(n) \cdot e^{-j\frac{2\cdot\pi\cdot k\cdot n}{N}}$$
$$Forward\ FFT\ x(n) = \frac{1}{N}\sum_{k=0}^{N-1} X(k) \cdot e^{j\frac{2\cdot\pi\cdot k\cdot n}{N}} \qquad (3)$$

542 where $x(n)$ indicates the periodic function, and *N* the number of samples within the
543 considered time window. For each *k*, the term constituted a harmonic component (the
544 complex version) with amplitude and frequency defined as:

545
$$Harmonic\ amplitude\ A_k = \frac{X(k)}{N}$$
$$Harmonic\ \ frequency\ \ f_k = \frac{F_s}{N} \qquad (4)$$

546 with F_s denoting the sampling frequency (0.5 KHz). The harmonic distortion values, which
547 indicated the harmonic content of a waveform compared to its fundamental, were
548 negligible. We calculated the **VOR gain** as the ratio between the first harmonic
549 amplitudes of the forward Fourier eye- and head-velocity transforms

550
$$VOR\ GAIN\ G = \frac{A_1^{eye-velocity}}{A_1^{head-velocity}} \qquad (5)$$

VOR protocols. In rotational chair testing, the subject (mouse, monkey, human) is seated on a rotatory table (Dumas et al., 2016). Speed and velocity of rotation are controlled and measured. The subject's head is restrained, assuming that the movement of the table equals to the subject's head movement. During normal VOR adaptation, a visual target is given in anti-phase with vestibular stimulation. The eyes must follow the visual target thus minimising the retinal slip. In the model, the eye output function was defined as:

$$\begin{aligned} Vestibular \quad stimulation &= sin\left(2 \cdot \pi \cdot t\right) \\ Eye\ output\ \ function &= A_E \cdot sin\left(2 \cdot \pi \cdot t + \pi \cdot \phi_E\right) \end{aligned} \tag{6}$$

where the ideal VOR experiment values corresponded to $A_E = -1, \phi_E = 0$ (visual field fixed).

Cerebellar Network Model

The cerebellar network model consisted of five neural populations (Fig. 1C).

Mossy fibres (MFs). 100 MFs constituted the input to the cerebellar network. Mossy fibres (MFs) conveyed the sensory signals from the vestibular organ and the eye muscles onto granule cells (GCs) and medial vestibular nuclei (MVN). MF activity evolved based on a sinusoidal function (1Hz with a step size of 0.002 ms) to encode head movements consistently with the functional principles of VOR control (Badura et al., 2016, Clopath et al., 2014, Arenz et al., 2008, Lisberger and Fuchs, 1978). MF responses consisted of non-overlapping activations of equally sized neural subpopulations, which maintained a constant overall firing rate (Luque et al., 2016).

Granular cells (GCs). 2000 GCs operated as a state generator (Yamazaki and Tanaka, 2007, Yamazaki and Tanaka, 2005, Yamazaki and Tanaka, 2009). In the presence of a constant MF input, the granular layer generated a sequence of non-overlapping

574 spatiotemporal patterns (i.e., states, Fujita, 1982). The same sequence of 500 states
575 (each consisting of 4 active GCs per time step of 2 ms) repeatedly activated every 1-sec
576 during learning (see below).

577 *Purkinje cells (PCs).* We modelled a population of 200 PCs, divided into 2 groups of 100
578 cells to control agonist and antagonist eye muscles, respectively. PCs integrated the
579 excitatory input from the parallel fibres (PFs), i.e. the axons of GCs, as well as the input
580 from the climbing fibres (CFs), i.e. the axons of inferior olive (IO) cells. PCs projected
581 inhibitory connections onto MVN cells, to close the cerebellar loop and generate the VOR
582 output.

583 *Inferior olive (IO) and climbing fibres (CFs).* We modelled 200 IO cells, divided in 2
584 groups of 100 IO cells for agonist/antagonist muscles, respectively. Each IO cell
585 projected a CF onto one PC and one MVN cell. IO cells were interconnected via
586 excitatory gap junctions, whose electrical coupling followed preferred directions (Devor
587 and Yarom, 2002). The preferred paths were disposed radially from the centre of 5x5 IO
588 cell subpopulations, as in a square regular lattice network (Nobukawa and Nishimura,
589 2016). The strength of the electrical coupling, which drove the recurrent dynamics of the
590 olivary population, was equal between all IO cells of the lattice network (see Table 1). In
591 terms of external inputs, the IO population received excitatory afferents coding for retina
592 slips (Clopath et al., 2014).This input reached the centre of each lattice network and it
593 was generated by a Poisson spiking process process (Boucheny et al., 2005, Luque et
594 al., 2011b). The IO population also received an inhibitory external input from MVN cells
595 (Fig. 1C) whose action regulated the IO network synchronisation via electrical coupling
596 modulation (Lefler et al., 2014, Best and Regehr, 2009). We assumed a progressive age-
597 related decrease of this inhibitory action based on the progressive age-loss of MVN
598 neurons (Torvik et al., 1986), which modulated the MVN-IO inhibitory synaptic weight

599 distribution of each 5x5 IO cell subpopulation. The variance of the Gaussian MVN-IO
600 weight distribution varied linearly from 0.4 to 1.75 causing a more homogeneous
601 electrical coupling along each 5x5 IO cell subpopulation whilst ageing.

602 The error-related inputs (coding for retina slips), combined with the recurrent electrical
603 coupling modulated by inhibitory MVN inputs, determined the overall activity of the IO
604 population, which generated the CF bursting output. The probabilistic spike sampling of
605 retina slips ensured an exploration of the whole error space over trials, whilst maintaining
606 the CF activity below 10 Hz per fibre (in agreement with electrophysiological data,
607 Kuroda et al., 2001). The evolution of the error could be sampled accurately even at
608 such a low frequency (Carrillo et al., 2008, Luque et al., 2011b). A graded representation
609 of the error signal (Najafi and Medina, 2013) led to a correlation between the intensity of
610 the sampled instantaneous error and the number of the spikes within the CF burst (Eq.
611 7):

$$s_{spikes} : [0,1] \subseteq \mathbb{R} \rightarrow \mathbb{R}$$
$$\varepsilon \rightarrow y = s_{spikes}(\varepsilon)$$

612
$$s_{spikes}(\varepsilon) = \begin{cases} 2 & if \quad 0.25 \le \varepsilon \le 0.50 \\ 3 & if \quad 0.50 \le \varepsilon \le 0.75 \\ 4 & if \quad 0.75 \le \varepsilon \le 0.85 \\ 5 & if \quad 0.85 \le \varepsilon \le 0.95 \\ 6 & if \quad 0.95 \le \varepsilon \le 1.0 \end{cases} \tag{7}$$

613 We assumed a perfect transmission of bursts from CFs to target PCs, i.e. the number of
614 spikes in a PC complex spike linearly depended on the number of spikes in the CF burst
615 (Mathy et al., 2009). The IO transmitted from 2 to 6 CF stimuli, delivered at inter-stimulus
616 intervals of 2 ms, a range representative of inter-spike intervals recorded in olivary axons
617 during bursts (Mathy et al., 2009, Davie et al., 2008), depending on the retina slips to be
618 compensated.

Medial Vestibular Nuclei (MVN) cells. We modelled a population of 200 MVN cells, with again 2 groups of 100 cells for agonist/antagonist muscles, respectively. Each MVN cell received an inhibitory afferent from a PC and an excitatory afferent from the IO cell that was also contacting that PC (Luque et al., 2014, Uusisaari and De Schutter, 2011). MVN cells also received excitatory projections from all MFs. The subcircuit IO-PC-MVN was then organised in a single microcomplex. This circuitry arrangement rested upon the principles of circuit integrity and uniformity on the olivo-cortico-nucleo-olivary loop (Uusisaari and De Schutter, 2011).

Translation of MVN spike trains into analogue eye motor commands. The MVN output was translated into analogue output signals by averaging the spiking activity of each MVN subpopulation (one for each agonist/antagonist group of muscles) (Eqs. 8, 9):

$$MVN_i(t) = \int_{t}^{t+T_{step}} \delta_{MVN_{spike}}(t) \cdot dt \tag{8}$$

$$MVN_{output}(t) = \alpha \left(\sum_{i=1}^{100} MVN_{ag,i}(t) - \sum_{j=1}^{100} MVN_{ant,j}(t) \right) \tag{9}$$

where α is the kernel amplitude that normalised the contribution of each MVN cell spike to the cerebellar output correction (the MVN_{ag} output controlled the agonist muscle, whilst the MVN_{ant} output controlled the antagonist muscle).

Table 1 summarises the parameters of the cerebellar topology used in the model.

***** *Table 1 about here* *****

Neuronal Models

MVN cell model. We modelled MVN cells as LIF neurons with excitatory (AMPA and NMDA) and inhibitory (GABA) chemical synapses (Eqs. 10-16).

$$C_m \cdot \frac{dV}{dt} = I_{leaky} + I_{external} \tag{10}$$

$$I_{leaky} = -g_L \cdot \left(V + E_L\right) \tag{11}$$

$$I_{external} = -\left(g_{AMPA}(t) + g_{NMDA}(t) \cdot g_{NMDA\_INF}\right) \cdot \left(V - E_{AMPA}\right) - -g_{GABA}(t) \cdot \left(V - E_{GABA}\right) \tag{12}$$

$$g_{AMPA}(t) = g_{AMPA}(t_0) \cdot e^{\frac{t-t_0}{\tau_{AMPA}}} + \sum_{i=1}^{N} \delta_{AMPA,i}(t) \cdot w_i \tag{13}$$

$$g_{NMDA}(t) = g_{NMDA}(t_0) \cdot e^{\frac{t-t_0}{\tau_{NMDA}}} + \sum_{i=1}^{N} \delta_{NMDA,i}(t) \cdot w_i \tag{14}$$

$$g_{GABA}(t) = g_{GABA}(t_0) \cdot e^{\frac{t-t_0}{\tau_{GABA}}} + \sum_{i=1}^{N} \delta_{GABA,i}(t) \cdot w_i \tag{15}$$

$$g_{NMDA\_INF} = \frac{1}{1 + e^{-62 \cdot V} \cdot \frac{1.2}{3.57}} \tag{16}$$

where: C_m denoted de membrane capacitance; V the membrane potential; I_{leaky} the leak current; $I_{external}$ the external currents; E_L the resting potential; g_L the conductance responsible for the passive decay term towards the resting potential; w_i the synaptic weight of the synapses between the neuron i and the target neuron. Conductances g_{AMPA}, g_{NMDA} and g_{GABA} integrated all the contributions received by each receptor (AMPA, NMDA, GABA) through individual synapses. These conductances were defined as decaying exponential functions, which were proportionally incremented via w_i upon each presynaptic spike arrival (Dirac delta function). Finally, g_{NMDA_INF} stand for the NMDA activation channel. Note that we set the neuron membrane potential to E_L during the refractory period (T_{ref}), just after reaching V_{thr} (votage firing threshold) (Gerstner and Kistler, 2002, Gerstner et al., 2014). All the parameters of the neuronal models are shown in Table 2.

***** ***Table 2 about here*** *****

Inferior olive (IO) neuronal model. We modelled IO cells as LIF neurons with excitatory (AMPA) and inhibitory (GABA) chemical synapses as well as with electronic gap junctions (Llinas et al., 1974, Sotelo et al., 1974) (Eqs. 17-22):

$$C_m \cdot \frac{dV}{dt} = I_{leaky} + I_{external} \tag{17}$$

$$I_{leaky} = -g_L \cdot \left(V + E_L\right) \tag{18}$$

$$\begin{aligned} I_{external} &= -g_{AMPA}\left(t\right) \cdot \left(V - E_{AMPA}\right) - \\ &-g_{GABA}\left(t\right) \cdot \left(V - E_{GABA}\right) - I_{EC} \end{aligned} \tag{19}$$

$$g_{AMPA}(t) = g_{AMPA}(t_0) \cdot e^{\frac{t-t_0}{\tau_{AMPA}}} + \sum_{i=1}^{N} \delta_{AMPA,i}(t) \cdot w_i \quad (20)$$

$$g_{GABA}(t) = g_{GABA}(t_0) \cdot e^{\frac{t-t_0}{\tau_{GABA}}} + \sum_{i=1}^{N} \delta_{GABA,i}(t) \cdot w_i \quad (21)$$

$$I_{EC} = \sum_{i=1}^{N} w_i \cdot (V - V_i) \cdot \left(0.6 \cdot e^{-\frac{(V-V_i)^2}{50^2}} + 0.4 \right) \quad (22)$$

where: C_m denotes de membrane capacitance; V the membrane potential; I_{leaky} the leak current; $I_{external}$ the external currents; E_L the resting potential; g_L the conductance responsible for the passive decay term toward the resting potential; w_i the synaptic weight of the synapses between the neuron *i* and the target neuron. Conductances g_{AMPA} and g_{GABA} integrated all the contributions received by each chemical receptor (AMPA, GABA) through individual synapses. These conductances were defined as decaying exponential functions, which were proportionally incremented via w_i upon each presynaptic spike arrival (Dirac delta function) (Gerstner and Kistler, 2002, Ros et al., 2006). I_{EC} represented the total current injected through the electrical synapses (Schweighofer et al., 1999). V was the membrane potential of the target neuron, V_i the membrane potential of the neuron *i, and N* was the total number of input synapses of the target neuron. Finally, for a correct operation of the electrical synapses, this model emulated the depolarisation and hyperpolarisation phases of an action potential. The LIF neuron incorporated a simple threshold process that enabled the generation of a triangular voltage function (maximum/minimum value V_{peak} /E_L respectively) each time the neuron fired (Bezzi et al., 2004). All the parameters of the IO neuronal model are shown in Table 2.

686 *Purkinje cell model*. The PC model was the same as in (Miyasho et al., 2001, Luque et
687 al., 2019, Middleton et al., 2008). It reproduced the three spiking modes of Purkinje cells,
688 namely tonic, bursting, and spike pauses (Forrest, 2008). The PC model consisted of a
689 single compartment with five ionic currents and two excitatory (AMPA) and inhibitory
690 (GABA) chemical synapses (Eqs. 23-27):

691 $$C_m \cdot \frac{dV}{dt} = I_{internal} + I_{external} \quad (23)$$

692 $$I_{internal} = -g_K \cdot n^4 \cdot (V+95) - g_{Na} \cdot m_0 [V]^3 \cdot h \cdot (V-50) - \\ -g_{Ca} \cdot c^2 \cdot (V-125) - g_L \cdot (V+70) - g_M \cdot M \cdot (V+95) \quad (24)$$

693 $$I_{external} = -g_{AMPA}(t) \cdot (V - E_{AMPA}) - g_{GABA}(t) \cdot (V - E_{GABA}) \quad (25)$$

694 $$g_{AMPA}(t) = g_{AMPA}(t_0) \cdot e^{\frac{t-t_0}{\tau_{AMPA}}} + \sum_{i=1}^{N} \delta_{AMPA,i}(t) \cdot w_i \quad (26)$$

695 $$g_{GABA}(t) = g_{GABA}(t_0) \cdot e^{\frac{t-t_0}{\tau_{GABA}}} + \sum_{i=1}^{N} \delta_{GABA,i}(t) \cdot w_i \quad (27)$$

696 where C_m denotes de membrane capacitance, V the membrane potential, I the internal
697 currents, $I_{external}$ the external currents, and w_i the synaptic weight of the synapses
698 between the neuron i and the target neuron. Conductances g_{AMPA} and g_{GABA} integrated
699 all the contributions received by each chemical receptor type (AMPA, GABA) through
700 individual synapses. These conductances were decaying exponential functions that were
701 proportionally incremented via w_i upon each presynaptic spike arrival (Dirac delta
702 function) (Ros et al., 2006, Gerstner and Kistler, 2002) . Finally, g_K was the delayed
703 rectifier potassium current, g_{Na} the transient inactivating sodium current, g_{Ca} the high-

threshold non-inactivating calcium current, g_L the leak current, and g_M the muscarinic receptor suppressed potassium current (see Table 3).

The dynamics of each gating variable (*n, h, c*, and *M*) followed the Eq. 28:

$$\dot{x} = \frac{x_0[V] - x}{\tau_x[V]} \tag{28}$$

where *x* corresponds to variables *n, h, c*, and *M*. The equilibrium function was given by the term $x_0[V]$ and the time constant $\tau_x[V]$ (see Table 3).

The sodium activation variable was replaced and approximated by its equilibrium function $m_0[V]$. The *M* current presented a temporal evolution significantly slower than the rest of variables. Each spike in the neuron generated a fast increase of the *M* current that took several milliseconds to return to its stable state. A high *M* current prevented the PC from entering in its tonic mode (when the neuron generated spikes due to PFs activity). A complex spike caused a rapid increase of the *M* current that depended, in turn, on the size of the spikelet within the burst. PC tonic mode resumed when the *M* current decreased.

We first validated the PC model in the NEURON simulator and then we reduced it to make it compatible with EDLUT (Luque et al., 2019). In the reduced PC model, we implemented the I_K and I_{Na} currents through a simple threshold process that triggered the generation of a triangular voltage function each time the neuron fired (Bezzi et al., 2004). This triangular voltage depolarisation drove the state of ion channels similarly to the original voltage depolarisation during the spike generation. The final internal current was given by Eq. 29:

$$I_{internal} = -g_{Ca} \cdot c^2 \cdot (V - 125) - g_L \cdot (V + 70) - g_M \cdot M \cdot (V + 95) \quad (29)$$

All the parameters are shown in Table 3.

***** Table 3 about here *****

Mossy fibres (MF) & granule cells (GC) models. MFs and GC neurons were simulated as leaky integrate–and–fire (LIF) neurons, with the same excitatory (AMPA) and inhibitory (GABA) chemical synapses and parameters as in (Luque et al., 2019).

Synaptic Plasticity Models

PC Intrinsic Plasticity. We equipped the PC model with a mechanism to update the value of the membrane capacitance (Cm) according to Eq. 30:

$$\frac{dC_m}{dt} = \frac{-\left(C_m - \frac{\beta}{2}\right)}{\beta \cdot \tau_{IP} \cdot (1 + I_{external})} \quad (30)$$

where τ_{IP} denotes the intrinsic plasticity time constant set to 12 10^3 sec (this large time constant prevented interferences between intrinsic plasticity and other STDP mechanisms during the learning process (Garrido et al., 2016); β controls the shape of the firing rate distribution and it is equal to 1 (see Garrido et al. (2016) for details about all intrinsic plasticity mechanism parameters). Whenever a spike was elicited, the C_m variable was updated according to the following equation:

$$\Delta C_m = \frac{\varepsilon_{Cm}}{\tau_{IP}} \quad if\ PC\ is\ active \quad (31)$$

where ε_{Cm} = 0.0475 (Garrido et al., 2016) determined the influence of each spike on C_m . Note that the membrane capacitance of PCs could not diminish below a lower limit (0.77 ± 0.17 μF cm−2 where mean ± s.d.; range, 0.64-1.00 μF cm−2; Roth and Häusser, 2001).

PF-PC synaptic plasticity. The model of long-term depression (LTD) and long-term potentiation (LTP) at PF–PC synapses was the same as in (Luque et al., 2019) and it followed the Eqs. 32 and 33:

$$LTD\ \Delta w_{PF_j-PC_i}(t) = \int_{-\infty}^{IO_{spike}} k\left(\frac{t - t_{IO_{spike}}}{\tau_{LTD}}\right) \cdot \delta_{GrC_{spike}}(t) \cdot dt \quad if\ PF_j\ is\ active\ at\ t \tag{32}$$

$$LTP\ \Delta w_{PF_j-PC_i}(t) = \alpha \quad const \tag{33}$$

where $\Delta w_{PF_j-PC_i}(t)$ denotes the weight change between the j^{th} PF and the target i^{th} PC; τ_{LTD} is the time constant that compensates for the sensory motor delay (i.e., about 100 ms, Sargolzaei et al., 2016); δ_{GrC} is the Dirac delta function corresponding to an afferent spike from a PF; and the kernel function *k(x)* is defined as in Eq. 34:

$$k(x) = e^{-x} \cdot sin(x)^{20} \tag{34}$$

With this parametric configuration, the effect on presynaptic spikes arriving through PFs is maximal over the 100 ms time window before CF spike arrival, thus accounting for the sensorimotor pathway delay. For the sake of computational efficiency, note that the

760 kernel $k(x)$ combines exponential and trigonometric functions that allow for recursive
761 computation suitable for an event-driven simulation scheme as EDLUT (Naveros et al.,
762 2017, Naveros et al., 2015, Ros et al., 2006). Computational recursion avoids integrating
763 the whole kernel upon each new spike arrival.

764 Finally, as shown in Eq. 33, the amount of LTP at PFs was fixed (Kawato and Gomi,
765 1992, Luque et al., 2016, Luque et al., 2011a), with an increase of synaptic efficacy equal
766 to α each time a spike arrived through a PF to the targeted PC. This STDP mechanism
767 correlated the activity patterns coming through the PFs to PCs with the instructive signals
768 coming from CFs to PCs (producing LTD in the activated PF–PC synapses). The
769 correlation process at PC level identified certain PF activity patterns and it consequently
770 reduced the PC output activity. A decrease of PC activations caused a subsequence
771 reduction on the PC inhibitory action over the target MVN. Since the MVN received an
772 almost constant gross MF activation, a lack of PC inhibitory action caused increasing
773 levels of MVN activation. Conversely, the STDP mechanism increased the PC inhibitory
774 activity by potentiating PF-PC synapses in the absence of instructive signal, thus causing
775 decreasing levels of MVN activations. Consequently, PC axon activity governed MVN
776 activation by shaping their inhibitory action produced onto MVN. This spike-timing-
777 dependent plasticity (STDP) mechanism, which regulated the LTP/LTD ration at PF-PC
778 synapses, shaped the inhibitory action of PCs onto MVN cells.

779 *MF-MVN synaptic plasticity.* The LTD/LTP dynamics at MF-MVN synapses were the
780 same as in Luque et al. (2019), i.e., they were based on the following rules:

781 $$LTD\ \Delta w_{MF_j-MVN_i}(t) = \int_{-\infty}^{\infty} k\left(\frac{t - t_{PC_{spike}}}{\sigma_{MF-MVN}}\right) \cdot \delta_{MF_{spike}}(t) \cdot dt \quad if\ MF_j\ is\ active\ at\ t$$

782 (35)

783 $$LTP\ \Delta w_{MF_j-MVN_i}(t) = \alpha \quad const \tag{36}$$

784 with $\Delta w_{MF_j-MVN_i}(t)$ denotes the weight change between the j^{th} MF and the target i^{th}

785 MVN; σ_{MF-MVN} the temporal width of the kernel; and δ_{MF} the Dirac delta function that

786 defined a MF spike. The integrative kernel function $k(x)$ was taken as:

787 $$k(x) = e^{-|x|} \cdot cos(x)^2 \tag{37}$$

788 Note that there is no need for sensorimotor delay compensation thanks to the previous

789 learning rule (τ_{LTD} in Eq. 32). This second STDP mechanism accounted for learning

790 consolidation at MVN (see Luque et al., 2016). The PC output operated as an

791 instructive signal and correlated the activity patterns coming from MFs to MVN

792 (producing LTD in the activated MF–MVN synapses upon the arrival of the instructive

793 signal and LTP otherwise). Well-timed sequences of increasing/decreasing levels of

794 MVN activation ultimately shaped the cerebellar output during VOR adaptation.

795 The EDLUT source code is available at the following URL:

796 www.ugr.es/~nluque/restringido/CODE_Cerebellar_Ageing_Vestibulo_Ocular_Adaptati

797 on.rar

798 User: REVIEWER, password: REVIEWER.

5. Figure Captions

Figure 1*| *Cerebellum-dependent adaptation of Vestibulo-Ocular Reflex (VOR). (A) *VOR stabilises the visual field during head motion, in this example during horizontal head rotations x(t), by producing contralateral eye movements y(t).* ***(B)*** *Cerebellar VOR adaptation was theoretically modelled in terms of a classic feedforward control loop. The control system compared a known reference, or input variable x(t) to the actual output y(t), to quantify an error signal $\varepsilon(t)$ driving adaptation. Cerebellar learning compensated for the difference between eye and head velocity (i.e., it minimised the error function $\varepsilon(t)$). The cerebellar model presented here had to learn contralateral eye control in the presence of a 1-Hz sinusoidal head velocity function (iteratively presented as in classical horizontal rotational VOR (i.e., r-VOR) (Leigh and Zee, 2015).* ***(C)*** *Schematic representation of the main cerebellar layers, cells, and synaptic connections considered in the model. Mossy fibres (MFs) conveyed vestibular information onto granular cells (GCs) and medial vestibular nuclei (MVN). GCs, in turn, projected onto Purkinje cells (PCs) through parallel fibres (PFs). PCs also received excitatory inputs from the inferior olivary (IO) system. IO cells were electrically coupled and delivered an error signal through the climbing fibres (CFs). Finally, MVN were inhibited by PCs and provide the cerebellar output driving oculomotor neurons. Two spike-dependent plasticity mechanisms operated at PF - PC and MF – MVN synapses.*

Figure 2*| *Time course of VOR gain and error during adaptation*. **(A)*** *Evolution of VOR gain averaged across 40 individuals with stochastically initialised weights at PF-PC and MF-MVN synapses, under a sinusoidal vestibular stimulus of 1 Hz. The gain plateaued at 0.95 in agreement with human records (Dits et al., 2013).* ***(B)*** *Red curve: convergence of the mean absolute VOR error during adaptation averaged over 40*

individuals. Green squares: error-related mean frequency of IO neurons throughout VOR adaptation (diminishing from 8-9 Hz to 2-3 Hz).

Figure 3| Impact of age-related vestibular loss on IO electrical coupling and cerebellar-dependent VOR adaptation. (A) *Mean frequency, averaged over 20 young (20 yo, top) and 20 older (100 yo, bottom) individuals, across a cluster of 5 × 5 IO cells (lattice configuration Nobukawa and Nishimura, 2016) during the first second of VOR adaptation under a sinusoidal vestibular stimulus of 1 Hz. Ageing engendered an on/off like transient pattern of IO network activity, leading to a higher average activation frequency in older IO cells.* ***(B)*** *Discrete Wavelet Transformation (DWT) applied to the snapshot sequence of the IO membrane potentials (Supp. Fig. 1A) obtained during the first second of VOR adaptation for a young (20 yo) and an older (100 yo) adult. In the presence of equivalent input stimulation to the IO network, the mean DWT coefficients were significantly higher in young adults (ANOVA $F_{(294,16)}=18$, $p < 10^{-7}$), indicating a more complex evolution of the spatial-temporal patterns, higher variability in membrane potentials, and lower overall frequencies in IO network activity.* ***(C)*** *Increase of the mean absolute VOR error (red curve) throughout ageing and corresponding increase of the average IO frequency (green squares), caused by altered electrical coupling (simulated from 40 to 100 years of age).* ***(D)*** *Age-related impact on VOR velocity compensatory eye velocity functions (with young and older IO network, red and black, respectively).* ***(E)*** *Cross-sectional ageing simulation over a study population of 2400 individuals aged from 40 to 100 years (40 individuals per each of year of age). Only the effect of age-related vestibular loss and IO coupling alteration was considered in this ageing simulation, with no compensatory mechanism operating in the downstream cerebellar network. Each individual underwent an independent 1 Hz r-VOR protocol (during 2500 s). On average,*

the VOR performance declined quasi-linearly throughout ageing, with an increasing interindividual variability.

Figure 4| Intrinsic plasticity at PC synapses as a local homeostatic mechanism. ***(A)*** *Trimodal spiking patterns of model PCs: tonic firing, corresponding to simple spikes elicited by PF inputs; bursting mode, during which complex spikes (bursts of spikes) are elicited by CFs (~500 synapses Palay and Chan-Palay, 2012) wrapping around PC dendrites that can even suppress simple spiking; and silent mode, corresponding to an extended hyperpolarisation period called the post-complex spike pause.* ***(B)*** *Intrinsic plasticity modified PC excitability through capacitance adaptation to age-dependent changes in the synaptic inputs (see Methods). The model PC capacitance decreased with ageing to facilitate neural excitability (Zhang et al., 2010)* ***(C)*** *As a consequence, PCs' firing rates increased significantly in older simulated individuals as compared to young ones (Zhang et al., 2010). This measure was realised with PCs operating in spiking tonic mode (10-250Hz).* ***(D)*** *The linear correlation between pause duration and pre-complex spike ISI duration (Grasselli et al., 2016) in older PCs was preserved (R^2 = 0.9932; $p < 10^{-4}$).* ***(E)*** *Cross-sectional ageing simulation accounting for vestibular loss, IO electrical coupling chances, and intrinsic plasticity at PC synapses. The VOR gain decayed linearly across the lifespan as in the previous ageing simulation. However, the adaptive excitability of PCs (induced by intrinsic plasticity) partially counterbalanced the vestibular degeneration (as compared to Fig. 3E).*

Figure 5| Spike-based plasticity mediating LTP/LTD at PF-PC and MF-MVN synapses. (A, B) *Synaptic weight distributions obtained at PF-PC connections by averaging over 20 young individuals (20 yo) and 20 older ones (100 yo), respectively. Each individual underwent an independent 1 Hz r-VOR adaptation (during 2500 s). The two cerebellar microcomplexes devoted to the control of rightward and leftward eye*

movements are visible. ***(C, D)*** *Synaptic weight distributions at MF-MVN connections by averaging over 20 young individuals (20 yo) and 20 older ones (100 yo), respectively. The antisymmetric distributions with respect to (A, B) are caused by the inhibitory PC projections onto MVN. To counter age-related afferent loss, LTP/LTD increased the weight of remaining synapses both at PF-PC and MF-MVN projections, significantly increasing the ratio between the number of saturated vs. active afferents. As a consequence, the neural drive increased significantly as a function of age.*

Figure 6| Cerebellar LTP/LTD as a global homeostatic compensatory mechanism. ***(A)*** *LTP/LTD sustained the input drive to PCs (computed by convolving unitary pulses and synaptic weight distributions) until about 80 years of age and it dropped afterwards.* ***(B)*** *A rapid boost of the neural drive at MVN synapses around 60 years of age helped maintaining the overall responses. Beyond 80 years of age, the neural drive could no longer be maintained against age-related vestibular losses.* ***(C)*** *Cross-sectional ageing simulation accounting for vestibular loss, IO electrical coupling alterations and LTP/LTD at PF-PC and MF-MVN synapses. The VOR performances remained quasi stable until about 80 years and it began to decline afterwards, with an incrementally increasing interindividual variability.*

Figure 7| Impact of ageing on VOR: cross-sectional and longitudinal studies. (A) *Cross-sectional ageing simulation accounting for all factors (vestibular loss, IO electrical coupling changes, PC intrinsic plasticity, and LTP/LTD at PF-PC and MF-MVN synapses) to evaluate their synergistic contribution to r-VOR adaptation. Again, a study population of 2400 individuals (age range: 40-100 years; 40 individuals per each year of age) underwent the same r-VOR protocol (1 Hz head rotation during 2500 s). The VOR gain remained quasi-stable until 80-85 yo, and it declined sharply afterwards.* ***(B)*** *The local homeostatic mechanism (PC intrinsic plasticity) helped sustaining the VOR gain*

further in age, complementing the global homeostatic action of LTP/LTD. ***(C)*** *The interindividual variability increased smoothly until 80-85 yo and it augmented rapidly afterwards, consistently with the tendency observed experimentally (Li et al., 2015).* ***(D)*** *Longitudinal ageing simulation considering all age-related and compensatory factors. A study population of 40 individuals were followed-up individually during 60 years (from 40 to 100 years of age) using the same r-VOR protocol (1 Hz head rotation during 2500 s). Age-related losses accumulated longitudinally for each individual. VOR performance remained quasi-stable until 80-85 yo and it declined sharply afterwards. Interindividual variability increased significantly during the last 15 years of age becoming larger than the one predicted by to the cross-sectional simulation (C). The thick green and red curves correspond to the 100 yo individuals with best and worst VOR performance, respectively.*

Figure 8| Distribution of remaining fibres/synaptic connections in the longitudinal ageing simulation. (A) *VOR gain at 100 years of age sorted incrementally across the study population. The red and green dots correspond to the worst and best individuals, respectively (i.e., red and green thick curves in Fig. 7D, respectively).* ***(B)*** *Eye velocity function, with a focus on time windows corresponding to the peak and the trough of the sinusoidal profile (i.e., between 200-300 ms and 700-800 ms).* ***(C)*** *Residual PFs (top) and MF-MVN projections (bottom) active at the peak and the trough of the eye velocity profile across all individuals sorted on the basis of their VOR performance (left: 60 yo; centre: at 85 yo; right: 100 yo). The larger the number of residual PFs and MV-MVN projections encoding the peak and the trough of the eye velocity function, the higher the VOR performance throughout ageing (see correlations in Supp. Fig. S2).*

Supplementary S1| Spatial-temporal evolution of the IO network activity patterns in young and older individuals. (A) *Spike propagation through electrical coupling along the diagonal of an IO cell cluster (5x5 lattice configuration) induced by an external*

stimulus delivered at the centre of the network. ***(B)*** *Time course of the membrane potentials of IO cells in 5x5 clusters caused by a large retinal slip (input stimulus received at the centre of the network at 1 ms) in young (top) and older (bottom) individuals.* ***(C)*** *Ageing favours a faster and higher electrical coupling in old adults.*

Supplementary S2| Correlation matrix between the VOR gain and the number of residual PFs and MF-MVN projections active at the peak and the trough of the eye velocity function. *The diagonal represents the histograms of the VOR performance values.*

6. Tables

Table 1. *Cerebellar network topology parameters*

Neurons		***Synapses***			
Pre-synaptic cells (number)	*Post-synaptic cells (number)*	*Number*	*Type*	*Initial weight*	*Weight range*
2000 GCs	*200 PCs*	*400000*	*AMPA*	*rand*	*[0, 3.65]*
200 IO	*200 PCs*	*200*	*AMPA*	*40*	*–*
100 MFs	*200 MVN*	*20000*	*AMPA*	*0*	*[0, 1]*
200 PCs	*200 MVN*	*200*	*GABA*	*1.5*	*–*
200 IO	*200 MVN*	*200*	*NMDA*	*7*	*–*
IO to IO (lattice configuration)		*320*	*EC*	*5*	*–*

Table 2. *Neuronal model parameters.*

Parameters	***MVN***	***IO***	***PC***
C_m ***(pF)***	*2*	*10*	*7.16*
G_L ***(nS)***	*0.2*	*0.15*	*0.15*
E_L ***(mV)***	*-70*	*-70*	*-70*
E_{AMPA} ***(mV)***	*0*	*0*	*0*
E_{GABA} ***(mV)***	*-80*	*-80*	*-80*
τ_{AMPA} ***(ms)***	*0.5*	*1*	*1*
τ_{NMDA} ***(ms)***	*14*		
τ_{GABA} ***(ms)***	*10*	*2*	*2*
V_{thr} ***(mV)***	*-40*	*-50*	*-35*
T_{ref} ***(ms)***	*1*	*1.35*	*1.35*

V_{peak} **(mV)**		31	31
gc_a **(mS)**			0.0075
g_M **(mS)**			5.65

934

935 **Table 3.** *Ionic conductance kinetic parameters.*

Conductance type	Steady–state Activation/Inactivation	Time constant (ms)
g_K delayed rectifier potassium current	$x_0[V] = \frac{1}{1+e^{\frac{-V-29.5}{10}}}$	$\tau_x[V] = 0.25 + 4.35 \cdot e^{\frac{-\lvert V+10\rvert}{10}}$
g_{Na} transient inactivating sodium current	$x_0[V] = \frac{1}{1+e^{\frac{V-59.4}{10.7}}}$	$\tau_x[V] = 0.15 + \frac{1.15}{1+e^{\frac{V+33.5}{15}}}$
$m_0[V]$	$m_0[V] = \frac{1}{1+e^{\frac{-V-48}{10}}} \cdot m$	
	Forward Rate Function (α)	**Backward Rate Function** (β)
g_{Ca} high threshold	$\alpha = \frac{1.6}{1+e^{-0.0072\cdot(V-5)}}$	$\beta = \frac{0.02\cdot(V+8.9)}{e^{\frac{V+8.9}{5}}}$
g_M muscarinic receptor suppressed potassium current	$\alpha = \frac{0.3}{1+e^{\frac{-V-2}{5}}}$	$\beta = 0.001 \cdot e^{\frac{-V-70}{18}}$
	Steady–state Activation/Inactivation	**Time constant(ms)**
	$x_0[V] = \frac{\alpha}{\alpha+\beta}$	$\tau_x[V] = \frac{1}{\alpha+\beta}$

936

937 7. References

938 AGRAWAL, Y., DAVALOS-BICHARA, M., ZUNIGA, M. G. & CAREY, J. P. 2013. Head
939 impulse test abnormalities and influence on gait speed and falls in older
940 individuals. *Otology & Neurotology,* 34**,** 1729-1735.

941 ALVAREZ, J. C., DíAZ, C., SUAREZ, C., FERNANDEZ, J. A., GONZALEZ DEL REY,
942 C., NAVARRO, A. & TOLIVIA, J. 2000. Aging and the human vestibular nuclei:
943 morphometric analysis. *Mechanisms of ageing and development,* 114**,** 149-72.
944 ALLEN, D., RIBEIRO, L., ARSHAD, Q. & SEEMUNGAL, B. M. 2017. Age-related
945 vestibular loss: current understanding and future research directions. *Frontiers in*
946 *neurology,* 7**,** 231.
947 ANDERSEN, B. B., GUNDERSEN, H. J. G. & PAKKENBERG, B. 2003. Aging of the
948 human cerebellum: a stereological study. *Journal of Comparative Neurology,*
949 466**,** 356-365.
950 ANSON, E. & JEKA, J. 2016. Perspectives on aging vestibular function. *Frontiers in*
951 *neurology,* 6**,** 269.
952 ANSON, E. R., BIGELOW, R. T., CAREY, J. P., XUE, Q.-L., STUDENSKI, S.,
953 SCHUBERT, M. C. & AGRAWAL, Y. 2016. VOR gain is related to compensatory
954 saccades in healthy older adults. *Frontiers in aging neuroscience,* 8**,** 150.
955 ARENZ, A., SILVER, R. A., SCHAEFER, A. T. & MARGRIE, T. W. 2008. The
956 Contribution of Single Synapses to Sensory Representation in Vivo. *Science* 321**,**
957 977-80.
958 ARLEO, A. & RONDI-REIG, L. 2007. Multimodal sensory integration and concurrent
959 navigation strategies for spatial cognition in real and artificial organisms. *Journal*
960 *of integrative neuroscience,* 6**,** 327-366.
961 BADURA, A., CLOPATH, C., SCHONEWILLE, M. & DE ZEEUW, C. I. 2016. Modeled
962 changes of cerebellar activity in mutant mice are predictive of their learning
963 impairments. *Sci. Rep.,* 6**,** 36131.
964 BALOH, R. W., ENRIETTO, J., JACOBSON, K. M. & LIN, A. 2001. Age-related changes
965 in vestibular function: a longitudinal study. *Annals of the New York Academy of*
966 *Sciences,* 942**,** 210-219.
967 BALOH, R. W., JACOBSON, K. M. & SOCOTCH, T. M. 1993. The effect of aging on
968 visual-vestibuloocular responses. *Exp. Brain Res.,* 95**,** 509-16.
969 BALOH, R. W., SLOANE, P. D. & HONRUBIA, V. 1989. Quantitative vestibular function
970 testing in elderly patients with dizziness. *Ear, nose, & throat journal,* 68**,** 935-9.
971 BERGSTRÖM, B. 1973. Morphology of the vestibular nerve: III. Analysis of the calibers
972 of the myelinated vestibular nerve fibers in man at various ages. *Acta oto-*
973 *laryngologica,* 76**,** 331-8.
974 BEST, A. R. & REGEHR, W. G. 2009. Inhibitory regulation of electrically coupled neurons
975 in the inferior olive is mediated by asynchronous release of GABA. *Neuron,* 62**,**
976 555-565.
977 BEZZI, M., NIEUS, T., COENEN, O. J.-M. D. & D'ANGELO, E. 2004. An I&F model of a
978 cerebellar granule cell. *Neurocomp.,* 58**,** 593-8.
979 BOUCHENY, C., CARRILLO, R. R., ROS, E. & COENEN, O. J.-M. D. 2005. Real-time
980 spiking neural network: an adaptive cerebellar model. *LNCS,* 3512**,** 136–44.
981 BRANDT, T., SCHAUTZER, F., HAMILTON, D. A., BRÜNING, R., MARKOWITSCH, H.
982 J., KALLA, R., DARLINGTON, C., SMITH, P. & STRUPP, M. 2005. Vestibular
983 loss causes hippocampal atrophy and impaired spatial memory in humans. *Brain,*
984 128**,** 2732-2741.
985 BRIZZEE, K. R., KAACK, B. & KLARA, P. 1975. Lipofuscin: intra-and extraneuronal
986 accumulation and regional distribution. *Neurobiology of Aging.* Springer.
987 CARRILLO, R. R., E. ROS, E., BOUCHENY, C. & COENEN, O. 2008. A real-time spiking
988 cerebellum model for learning robot control. *Biosystems,* 94**,** 18-27.
989 CLOPATH, C., BADURA, A., DE ZEEUW, C. I. & BRUNEL, N. 2014. A cerebellar
990 learning model of VOR adaptation in wild-type and mutant mice. *J. Neurosci.,* 34**,**
991 7203-15.

CULLEN, K. E. 2012. The vestibular system: multimodal integration and encoding of self-motion for motor control. *Trends in neurosciences,* 35**,** 185-196.

D'ANGELO, E. & DE ZEEUW, C. I. 2009. Timing and plasticity in the cerebellum: focus on the granular layer. *Trends Neurosci.,* 32**,** 10.

D'ANGELO, E., MAPELLI, L., CASELLATO, C., GARRIDO, J. A., LUQUE, N., MONACO, J., PRESTORI, F., PEDROCCHI, A. & ROS, E. 2016. Distributed circuit plasticity: new clues for the cerebellar mechanisms of learning. *The Cerebellum,* 15**,** 139-151.

DAVIE, J. T., CLARK, B. A. & HÄUSSER, M. 2008. The origin of the complex spike in cerebellar Purkinje cells. *J. Neurosci.,* 28**,** 7599-7609.

DE ZEEUW, C. I., HOOGENRAAD, C. C., KOEKKOEK, S. K. E., RUIGROK, T. J., GALJART, N. & SIMPSON, J. I. 1998. Microcircuitry and function of the inferior olive. *Trends Neurosci.,* 21**,** 391-400.

DEMER, J. L., HONRUBIA, V. & BALOH, R. W. 1994. Dynamic visual acuity: a test for oscillopsia and vestibulo-ocular reflex function. *The American journal of otology,* 15**,** 340-347.

DEMER, J. L., OAS, J. G. & BALOH, R. W. 1993. Visual-vestibular interaction in humans during active and passive, vertical head movement. *J. Vestib. Res.,* 3**,** 101-14.

DENG, Y., XU, L., ZENG, X., LI, Z., QIN, B. & HE, N. 2010. New perspective of GABA as an inhibitor of formation of advanced lipoxidation end-products: it's interaction with malondiadehyde. *J Biomed Nanotechnol,* 6**,** 318-24.

DESAI, A., GOODMAN, V., KAPADIA, N., SHAY, B. L. & SZTURM, T. 2010. Relationship between dynamic balance measures and functional performance in community-dwelling elderly people. *Physical therapy,* 90**,** 748-760.

DEVOR, A. & YAROM, Y. 2002. Generation and propagation of subthreshold waves in a network of inferior olivary neurons. *Journal of neurophysiology,* 87**,** 3059-3069.

DITS, J., HOUBEN, M. M. & VAN DER STEEN, J. 2013. Three dimensional Vestibular ocular reflex testing using a Six degrees of freedom motion platform. *JoVE (Journal of Visualized Experiments)***,** e4144.

DUMAS, G., PERRIN, P., OUEDRAOGO, E. & SCHMERBER, S. 2016. How to perform the skull vibration-induced nystagmus test (SVINT). *European annals of otorhinolaryngology, head and neck diseases,* 133**,** 343-348.

FONSECA, D. B., SHEEHY, M. R. J., BLACKMAN, N., SHELTON, P. M. J. & PRIOR, A. E. 2005. Reversal of a hallmark of brain ageing: lipofuscin accumulation. *Neurobiol. Aging,* 26**,** 69-76.

FORREST, M. 2008. *Biophysics of Purkinje computation.* University of Warwick.

FUJITA, M. 1982. Adaptive filter model of the cerebellum. *Biological cybernetics,* 45**,** 195-206.

FURMAN, J. M. & REDFERN, M. S. 2001. Effect of aging on the otolith-ocular reflex. *Journal of Vestibular Research,* 11**,** 91-103.

GAO, Z., VANBEUGEN, B. J. & DE ZEEUW, C. I. 2012. Distributed Synergistic Plasticity and Cerebellar Learning. *Nat. Rev. Neurosci.,* 13**,** 1-17.

GARRIDO, J. A., LUQUE, N. R., TOLU, S. & D'ANGELO, E. 2016. Oscillation-driven spike-timing dependent plasticity allows multiple overlapping pattern recognition in inhibitory interneuron networks. *Int. J. Neural Systems,* 26**,** 1650020.

GERSTNER, W. & KISTLER, W. M. 2002. *Spiking neuron models: Single neurons, populations, plasticity*, Cambridge university press.

GERSTNER, W., KISTLER, W. M., NAUD, R. & PANINSKI, L. 2014. *Neuronal dynamics: From single neurons to networks and models of cognition*, Cambridge University Press.

GORDON, J. L., FURMAN, J. M. R. & KAMEN, E. W. System identification of the vestibulo-ocular reflex: application of the recursive least-squares algorithm. Bioengineering Conference, 1989., Proceedings of the 1989 Fifteenth Annual Northeast, 1989. IEEE, 199-200.

GRASSELLI, G., HE, Q., WAN, V., ADELMAN, J. P., OHTSUKI, G. & HANSEL, C. 2016. Activity-Dependent Plasticity of Spike Pauses in Cerebellar Purkinje Cells. *Cell Reports,* 14**,** 2546-53.

GROSSMAN, G. E. & LEIGH, R. J. 1990. Instability of gaze during locomotion in patients with deficient vestibular function. *Annals of Neurology: Official Journal of the American Neurological Association and the Child Neurology Society,* 27**,** 528-532.

HIRVONEN, T., AALTO, H., PYYKKÖ, I., JUHOLA, M. & JÄNTTIL, P. 1997. Changes in vestibulo-ocular reflex of elderly people. *Acta Oto-Laryngologica,* 117**,** 108-110.

HORAK, F. B. 2006. Postural orientation and equilibrium: what do we need to know about neural control of balance to prevent falls? *Age and ageing,* 35**,** ii7-ii11.

ICHIKAWA, R., SAKIMURA, K. & WATANABE, M. 2016. GluD2 endows parallel fiber–Purkinje cell synapses with a high regenerative capacity. *Journal of neuroscience,* 36**,** 4846-4858.

ISHIKAWA, T., SHIMUTA, M. & HÄUSSER, M. 2015. Multimodal sensory integration in single cerebellar granule cells in vivo. *Elife,* 4**,** e12916.

ITO, M. 2013. Error Detection and Representation in the Olivo-Cerebellar System. *Front. Neural Circuits***,** 1-8.

JAHN, K., NAEßL, A., SCHNEIDER, E., STRUPP, M., BRANDT, T. & DIETERICH, M. 2003. Inverse U-shaped curve for age dependency of torsional eye movement responses to galvanic vestibular stimulation. *Brain,* 126**,** 1579-1589.

JANG, D. C., SHIM, H. G. & KIM, S. J. 2020. Intrinsic plasticity of cerebellar purkinje cells contributes to motor memory consolidation. *Journal of Neuroscience,* 40**,** 4145-4157.

KAWATO, M. & GOMI, H. 1992. A computational model of four regions of the cerebellum based on FEL. *Biol. Cybern.,* 68**,** 95-103.

KURODA, S., YAMAMOTO, K., MIYAMOTO, H., DOYA, K. & KAWATO, M. 2001. Statistical characteristics of climbing fiber spikes necessary for efficient cerebellar learning. *Biol. Cybern.,* 84**,** 183-92.

LACKNER, J. R. & DIZIO, P. 2005. Vestibular, proprioceptive, and haptic contributions to spatial orientation. *Annu. Rev. Psychol.,* 56**,** 115-147.

LASN, H., WINBLAD, B. & BOGDANOVIC, N. 2001. The number of neurons in the inferior olivary nucleus in Alzheimer's disease and normal aging: A stereological study using the optical fractionator. *J. Alzheimer's Disease,* 3**,** 159-68.

LATORRE, R., AGUIRRE, C., RABINOVICH, M. & VARONA, P. 2013. Transient dynamics and rhythm coordination of inferior olive spatio-temporal patterns. *Frontiers in Neural Circuits,* 7.

LEFLER, Y., AMSALEM, O., VRIELER, N., SEGEV, I. & YAROM, Y. 2020. Using subthreshold events to characterize the functional architecture of the electrically coupled inferior olive network. *Elife,* 9**,** e43560.

LEFLER, Y., YAROM, Y. & UUSISAARI, M. Y. 2014. Cerebellar inhibitory input to the inferior olive decreases electrical coupling and blocks subthreshold oscillations. *Neuron,* 81**,** 1389-400.

LEIGH, R. J. & ZEE, D. S. 2015. *The neurology of eye movements*, Oxford University Press.

LI, C., LAYMAN, A. J., GEARY, R., ANSON, E., CAREY, J. P., FERRUCCI, L. & AGRAWAL, Y. 2015. Epidemiology of vestibulo-ocular reflex function: data from the Baltimore Longitudinal Study of Aging. *Otol Neurotol,* 36**,** 267-72.

LI, C. & LI, Y. 2013. A spike-based model of neuronal intrinsic plasticity. *IEEE Trans. Autonomous Mental Develop.,* 5**,** 62-73.

LISBERGER, S. G. & FUCHS, A. F. 1978. Role of primate flocculus during rapid behavioral modification of VOR. II. Mossy fiber firing patterns during horizontal head rotation and eye movement. *J. Neurophysiol.,* 41**,** 764-77.

LOEWENSTEIN, Y. 2002. A possible role of olivary gap-junctions in the generation of physiological and pathological tremors. *Mol. Psychiatry,* 7**,** 129.

LOPEZ, I., HONRUBIA, V. & BALOH, R. W. 1996. Aging and the human vestibular nucleus. *J. Vestibular research: equilibrium & orientation,* 7**,** 77-85.

LORENTE DE NÓ, R. 1933. Vestibulo-ocular reflex arc. *Archiv Neurol & Psychiatry*.

LUQUE, N. R., GARRIDO, J. A., CARRILLO, R. R., COENEN, O. J. M. D. & ROS, E. 2011a. Cerebellar Input Configuration Toward Object Model Abstraction in Manipulation Tasks. *IEEE Trans. Neural. Netw.,* 22**,** 1321-8.

LUQUE, N. R., GARRIDO, J. A., CARRILLO, R. R., COENEN, O. J. M. D. & ROS, E. 2011b. Cerebellarlike Corrective Model Inference Engine for Manipulation Tasks. *IEEE Trans. Syst. Man. Cybern.,* 41**,** 1299-312.

LUQUE, N. R., GARRIDO, J. A., CARRILLO, R. R., D'ANGELO, E. & ROS, E. 2014. Fast convergence of learning requires plasticity between inferior olive and deep cerebellar nuclei in a manipulation task: a closed-loop robotic simulation. *Front. Comput. Neurosci.,* 8.

LUQUE, N. R., GARRIDO, J. A., NAVEROS, F., CARRILLO, R. R., D'ANGELO, E. & ROS, E. 2016. Distributed Cerebellar Motor Learning; a STDP Model. *Front. Comp. Neurosci.,* 10.

LUQUE, N. R., NAVEROS, F., CARRILLO, R. R., ROS, E. & ARLEO, A. 2019. Spike burst-pause dynamics of Purkinje cells regulate sensorimotor adaptation. *PLOS Computational Biology,* 15**,** e1006298.

LLINAS, R., BAKER, R. & SOTELO, C. 1974. Electrotonic coupling between neurons in cat inferior olive. *J. Neurophysiol.,* 37**,** 560-71.

MATHY, A., HO, S. S., DAVIE, J. T., DUGUID, I. C., CLARK, B. A. & HAUSSER, M. 2009. Encoding of oscillations by axonal bursts in inferior olive neurons. *Neuron,* 62**,** 388-99.

MATIÑO-SOLER, E., ESTELLER-MORE, E., MARTIN-SANCHEZ, J.-C., MARTINEZ-SANCHEZ, J.-M. & PEREZ-FERNANDEZ, N. 2015. Normative data on angular vestibulo-ocular responses in the yaw axis measured using the video head impulse test. *Otology & Neurotology,* 36**,** 466-471.

MCGARVIE, L. A., MACDOUGALL, H. G., HALMAGYI, G. M., BURGESS, A. M., WEBER, K. P. & CURTHOYS, I. S. 2015. The video head impulse test (vHIT) of semicircular canal function–age-dependent normative values of VOR gain in healthy subjects. *Frontiers in neurology,* 6**,** 154.

MERGNER, T. & ROSEMEIER, T. 1998. Interaction of vestibular, somatosensory and visual signals for postural control and motion perception under terrestrial and microgravity conditions—a conceptual model. *Brain research reviews,* 28**,** 118-135.

MIDDLETON, S. J., RACCA, C., CUNNINGHAM, M. O., TRAUB, R. D., MONYER, H., KNOPFEL, T., SCHOFIELD, I. S., JENKINS, A. & WHITTINGTON, M. A. 2008. High-frequency network oscillations in cerebellar cortex. *Neuron,* 58**,** 763-74.

MIYASHO, T., TAKAGI, H., SUZUKI, H., WATANABE, S., INOUE, M., KUDO, Y. & MIYAKAWA, H. 2001. Low-threshold potassium channels and a low-threshold

calcium channel regulate Ca2+ spike firing in the dendrites of cerebellar Purkinje neurons: a modeling study. *Brain Res.,* 891**,** 106-15.

NAJAC, M. & RAMAN, I. M. 2015. Integration of Purkinje Cell Inhibition by Cerebellar Nucleo-Olivary Neurons. *J. Neurosci.,* 35**,** 544-9.

NAJAFI, F. & MEDINA, J. F. 2013. Beyond "all-or-nothing" climbing fibers: graded representation of teaching signals in Purkinje cells. *Front. Neural Circuits,* 7**,** 1-15.

NAVEROS, F., GARRIDO, J. A., CARRILLO, R. R., ROS, E. & LUQUE, N. R. 2017. Event-and Time-Driven Techniques Using Parallel CPU-GPU Co-processing for Spiking Neural Networks. *Front. Neuroinformatics,* 11.

NAVEROS, F., LUQUE, N. R., GARRIDO, J. A., CARRILLO, R. R., ANGUITA, M. & ROS, E. 2015. A Spiking Neural Simulator Integrating Event-Driven and Time-Driven Computation Schemes Using Parallel CPU-GPU Co-Processing: A Case Study. *IEEE Trans. Neural Netw. Learn. Syst.,* 26**,** 1567-74.

NAVEROS, F., LUQUE, N. R., ROS, E. & ARLEO, A. 2019. VOR Adaptation on a Humanoid iCub Robot Using a Spiking Cerebellar Model. *IEEE transactions on cybernetics*.

NGUYEN-VU, T. B., ZHAO, G. Q., LAHIRI, S., KIMPO, R. R., LEE, H., GANGULI, S., SHATZ, C. J. & RAYMOND, J. L. 2017. A saturation hypothesis to explain both enhanced and impaired learning with enhanced plasticity. *elife,* 6**,** e20147.

NOBUKAWA, S. & NISHIMURA, H. 2016. Chaotic resonance in coupled inferior olive neurons with the Llinás approach neuron model. *Neural computation,* 28**,** 2505-2532.

PAIGE, G. 1992. Senescence of human visual-vestibular interactions. 1. Vestibulo-ocular reflex and adaptive plasticity with aging. *Journal of vestibular research: equilibrium & orientation,* 2**,** 133-151.

PAIGE, G. D. 1994. Senescence of human visual-vestibular interactions: smooth pursuit, optokinetic, and vestibular control of eye movements with aging. *Experimental brain research,* 98**,** 355-372.

PALAY, S. L. & CHAN-PALAY, V. 2012. *Cerebellar cortex: cytology and organization*, Springer Science & Business Media.

PERNICE, H. F., SCHIEWECK, R., JAFARI, M., STRAUB, T., BILBAN, M., KIEBLER, M. A. & POPPER, B. 2019. Altered Glutamate Receptor Ionotropic Delta Subunit 2 Expression in Stau2-Deficient Cerebellar Purkinje Cells in the Adult Brain. *International journal of molecular sciences,* 20**,** 1797.

PETERKA, R. J., BLACK, F. O. & SCHOENHOFF, M. B. 1990. Age-related changes in human vestibulo-ocular reflexes: sinusoidal rotation and caloric tests. *J Vestib Res,* 1**,** 49-59.

PIIRTOLA, M. & ERA, P. 2006. Force platform measurements as predictors of falls among older people–a review. *Gerontology,* 52**,** 1-16.

RENOVELL, A., GINER, J. & PORTOLES, M. 2001. Loss of granule neurons in the aging human cerebellar cortex. *International Journal of Developmental Biology,* 40**,** S193-S194.

ROBINSON, D. A. 1981. The use of control systems analysis in the neurophysiology of eye movements. *Annual review of neuroscience,* 4**,** 463-503.

ROS, E., CARRILLO, R. R., ORTIGOSA, E. M., BARBOUR, B. & AGÍS, R. 2006. Event-driven simulation scheme for spiking neural networks using lookup tables to characterize neuronal dynamics. *Neural Comput.,* 18**,** 2959-93.

ROTH, A. & HÄUSSER, M. 2001. Compartmental models of rat cerebellar Purkinje cells based on simultaneous somatic and dendritic patch-clamp recordings. *J. Physiol.,* 535**,** 445-72.

SANTINA, C. C., CREMER, P. D., CAREY, J. P. & MINOR, L. B. 2001. The Vestibulo-Ocular Reflex during Self-Generated Head Movements by Human Subjects with Unilateral Vestibular Hypofunction. *Annals New York Academy of Sciences,* 942**,** 465-6.

SARGOLZAEI, A., ABDELGHANI, M., YEN, K. K. & SARGOLZAEI, S. 2016. Sensorimotor control: computing the immediate future from the delayed present. *BMC bioinformatics,* 17**,** 245.

SCHWEIGHOFER, N., DOYA, K. & KAWATO, M. 1999. Electrophysiological properties of inferior olive neurons: a compartmental model. *Journal of neurophysiology,* 82**,** 804-817.

SCHWEIGHOFER, N., LANG, E. J. & KAWATO, M. 2013. Role of the olivo-cerebellar complex in motor learning and control. *Frontiers in neural circuits,* 7**,** 94.

SHIM, H. G., JANG, D. C., LEE, J., CHUNG, G., LEE, S., KIM, Y. G., JEON, D. E. & KIM, S. J. 2017. Long-term depression of intrinsic excitability accompanied by the synaptic depression in the cerebellar Purkinje cells. *J. Neurosci.***,** 3464-16.

SHIM, H. G., LEE, Y.-S. & KIM, S. J. 2018. The emerging concept of intrinsic plasticity: activity-dependent modulation of intrinsic excitability in cerebellar Purkinje cells and motor learning. *Experimental neurobiology,* 27**,** 139.

SKAVENSKI, A. A. & ROBINSON, D. A. 1973. Role of abducens neurons in vestibuloocular reflex. *Journal of Neurophysiology,* 36**,** 724-738.

SOTELO, C., LLINAS, R. & BAKER, R. 1974. Structural study of inferior olivary nucleus of the cat: morphological correlates of electrotonic coupling. *J. Neurophysiol.,* 37**,** 541-59.

SULZER, D., MOSHAROV, E., TALLOCZY, Z., ZUCCA, F. A., SIMON, J. D. & ZECCA, L. 2008. Neuronal pigmented autophagic vacuoles: lipofuscin, neuromelanin, and ceroid as macroautophagic responses during aging and disease. *J. Neurochem.,* 106**,** 24-36.

TINETTI, M. E. 2003. Preventing falls in elderly persons. *New England journal of medicine,* 348**,** 42-49.

TOKUDA, I. T., HOANG, H., SCHWEIGHOFER, N. & KAWATO, M. 2013. Adaptive coupling of inferior olive neurons in cerebellar learning. *Neural Networks,* 47**,** 42-50.

TORVIK, A., TORP, S. & LINDBOE, C. 1986. Atrophy of the cerebellar vermis in ageing: a morphometric and histologic study. *Journal of the neurological sciences,* 76**,** 283-294.

TURRIGIANO, G., ABBOTT, L. F. & MARDER, E. 1994. Activity-dependent changes in the intrinsic properties of cultured neurons. *Science,* 264**,** 974-6.

UUSISAARI, M. & DE SCHUTTER, E. 2011. The mysterious microcircuitry of the cerebellar nuclei. *The Journal of physiology,* 589**,** 3441-3457.

VISWASOM, A. A., SIVAN, S. & JOBBY, A. 2013. Age related changes in the granule cell number in the human cerebellar cortex. *Journal of Evolution of Medical and Dental Sciences,* 2**,** 2698-2705.

YAMAZAKI, T. & TANAKA, S. 2005. Neural modeling of an internal clock. *Neural Comput,* 17**,** 1032-58.

YAMAZAKI, T. & TANAKA, S. 2007. The cerebellum as a liquid state machine. *Neural Netw.,* 20**,** 290-7.

YAMAZAKI, T. & TANAKA, S. 2009. Computational models of timing mechanisms in the cerebellar granular layer. *Cerebellum,* 8**,** 423-32.

YIN, D. 1996. Biochemical basis of lipofuscin, ceroid, and age pigment-like fluorophores. *Free Radical Biology and Medicine,* 21**,** 871-888.

YUZAKI, M. 2013. Cerebellar LTD vs. motor learning—lessons learned from studying GluD2. *Neural networks,* 47**,** 36-41.

ZALEWSKI, C. K. Aging of the human vestibular system. Seminars in hearing, 2015. Thieme Medical Publishers, 175-196.

ZANJANI, H. S., VOGEL, M. W. & MARIANI, J. 2016. Deletion of the GluRδ2 receptor in the hotfoot mouse mutant causes granule cell loss, delayed Purkinje cell death, and reductions in Purkinje cell dendritic tree area. *The Cerebellum,* 15**,** 755-766.

ZHANG, C., ZHU, Q. & HUA, T. 2010. Aging of cerebellar Purkinje cells. *Cell and tissue research,* 341**,** 341-7.

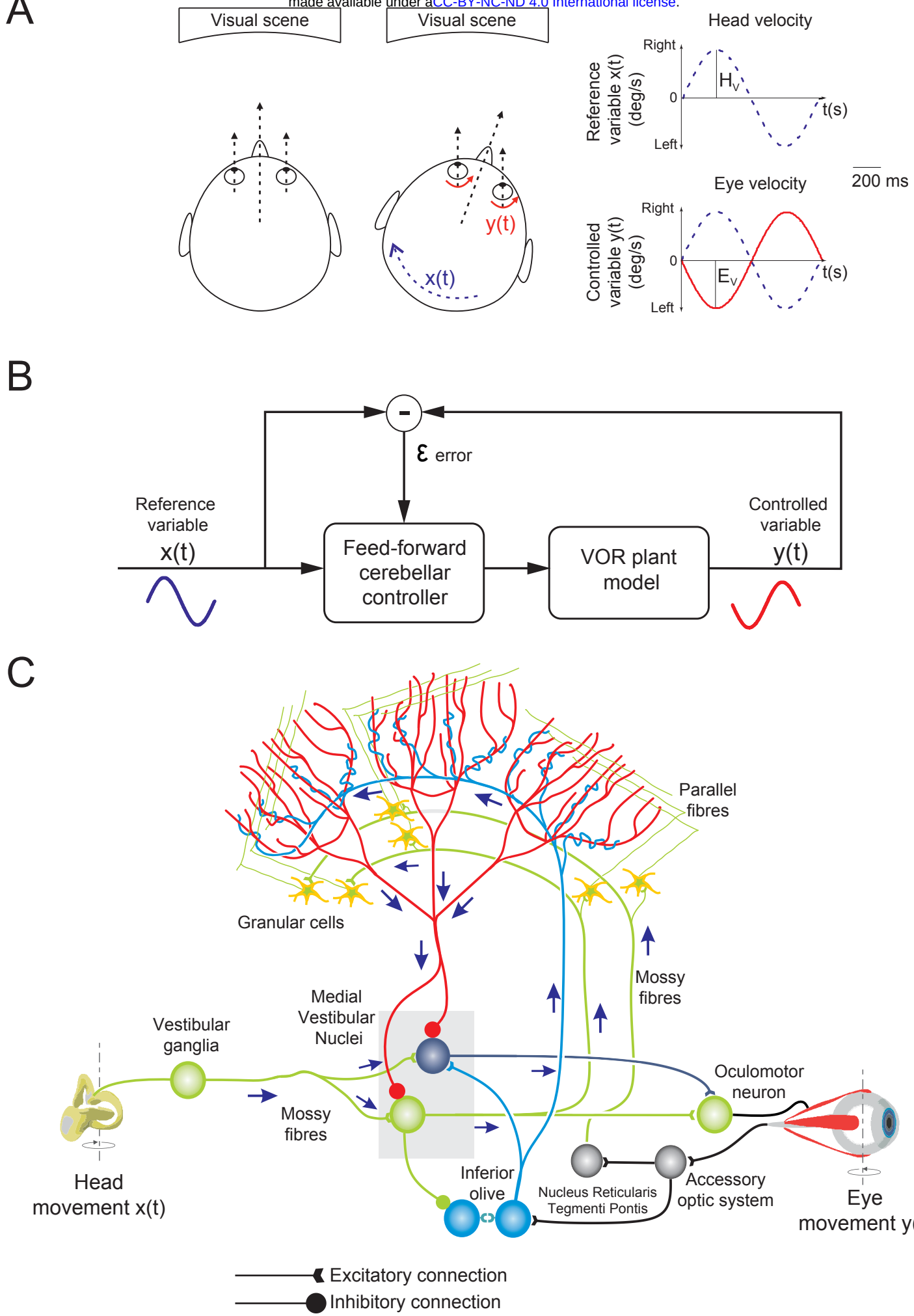

Figure 1

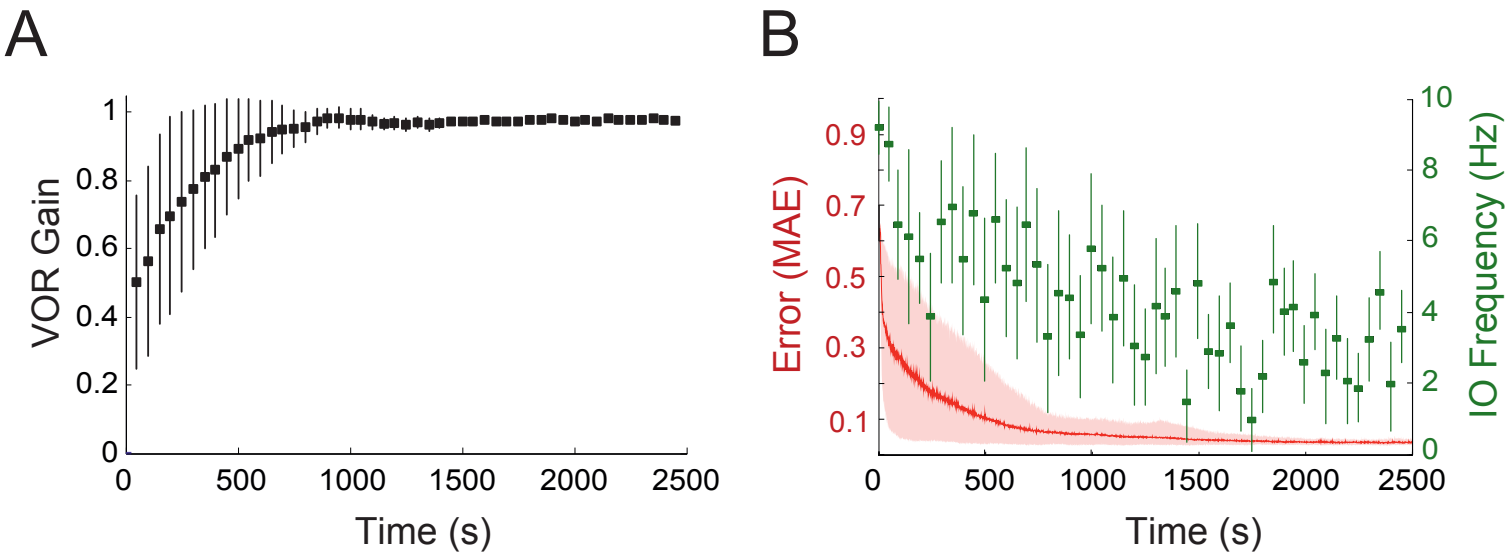

Figure 2

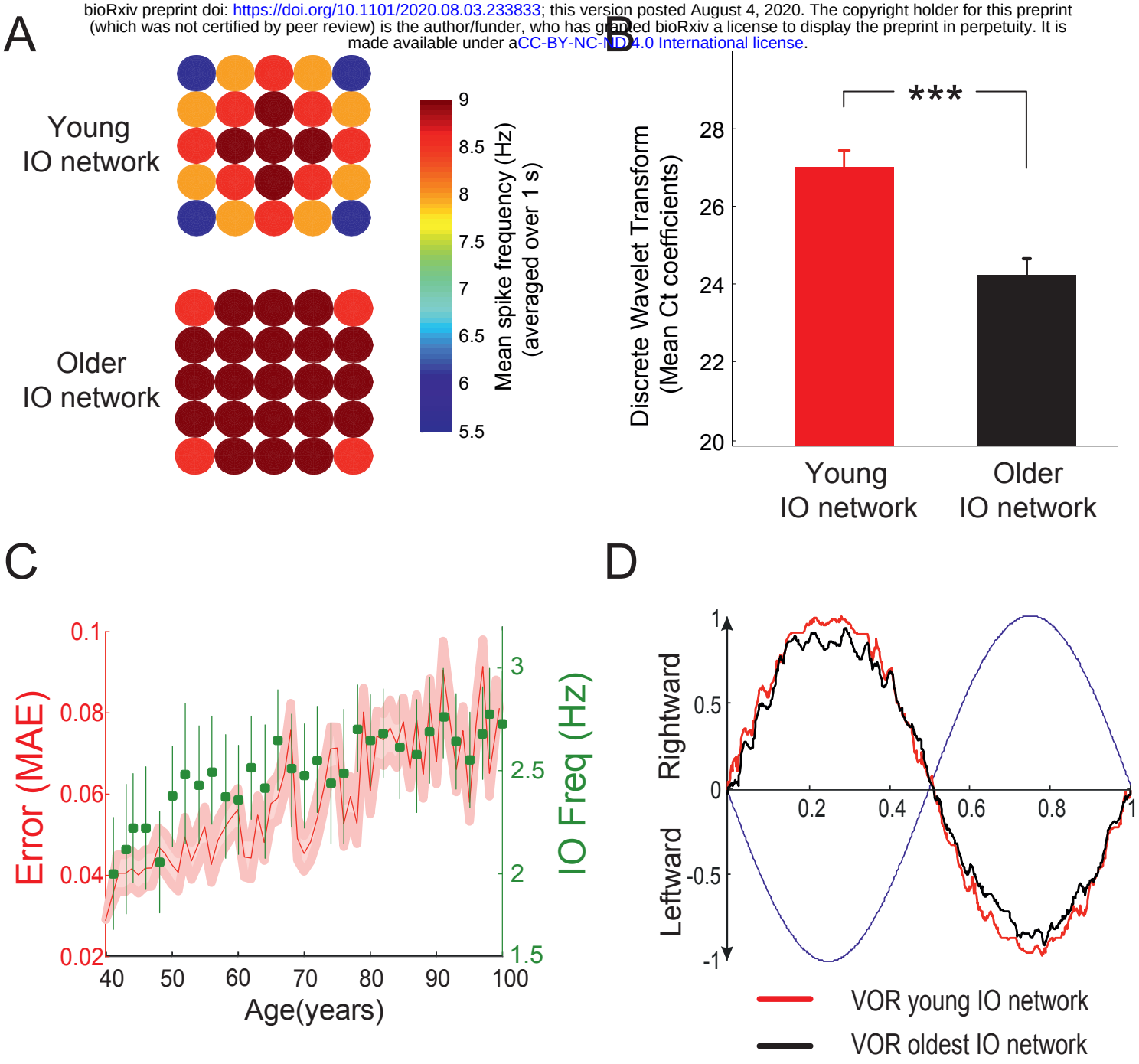

Figure 3

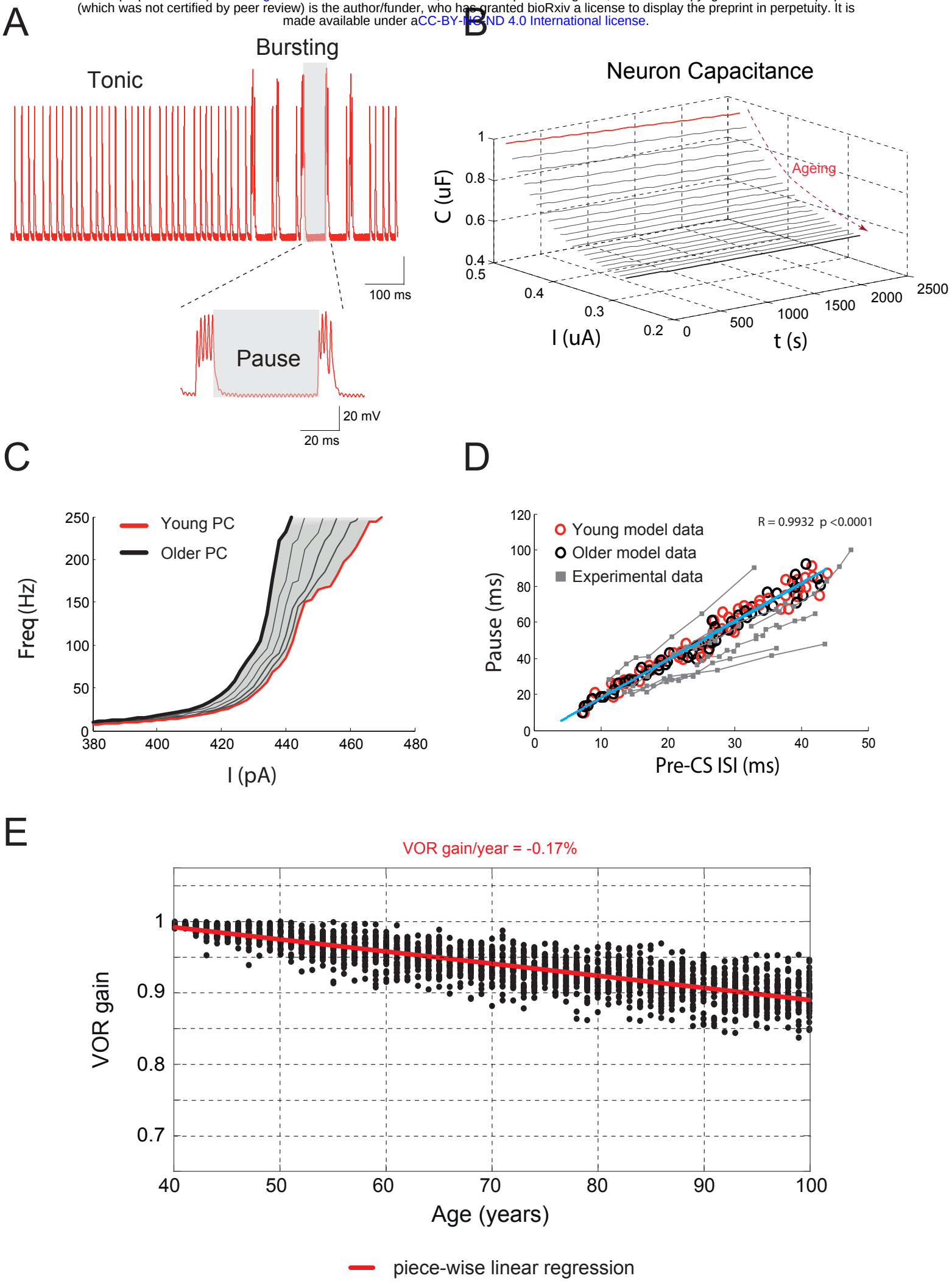

Figure 4

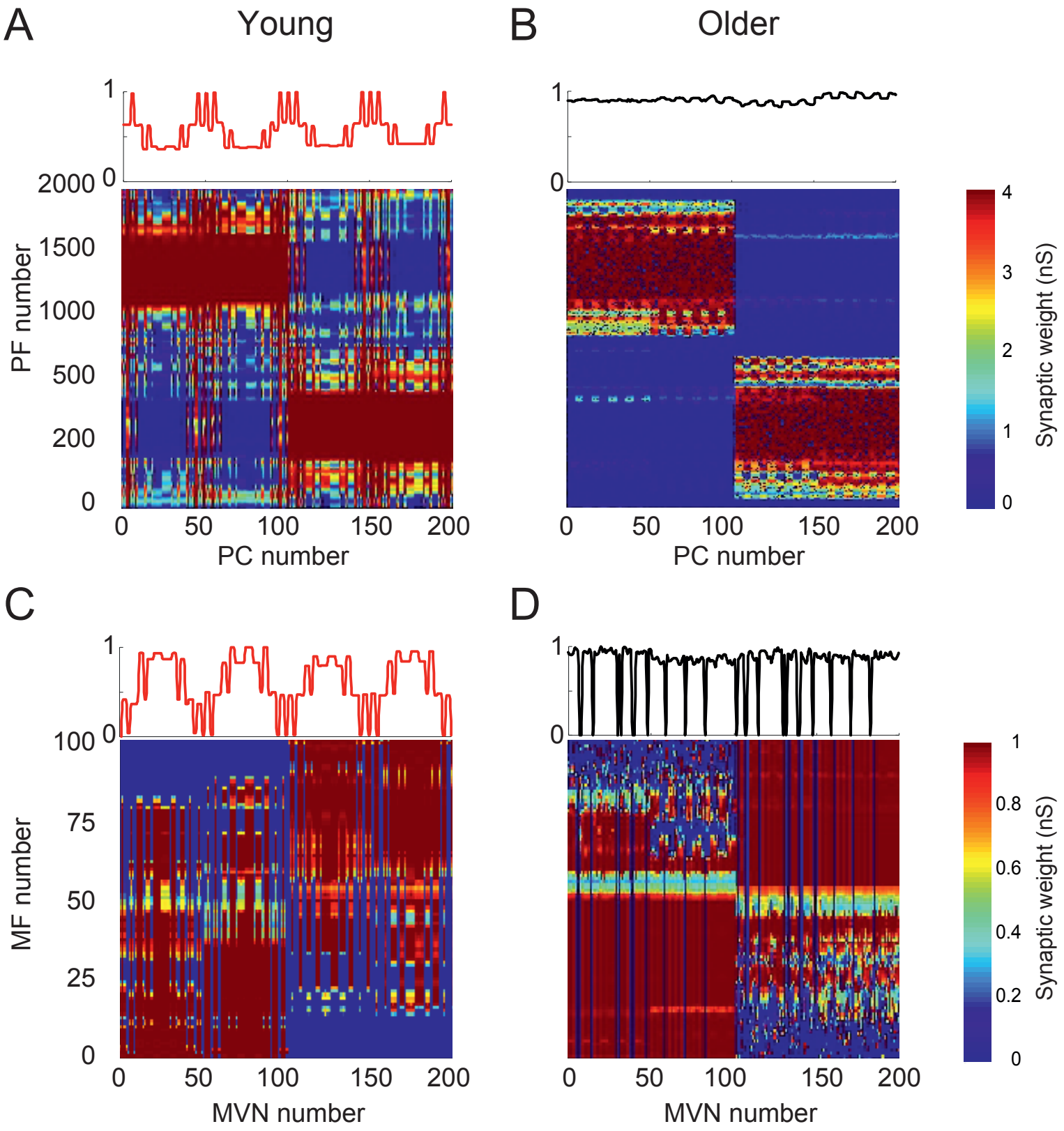

Figure 5

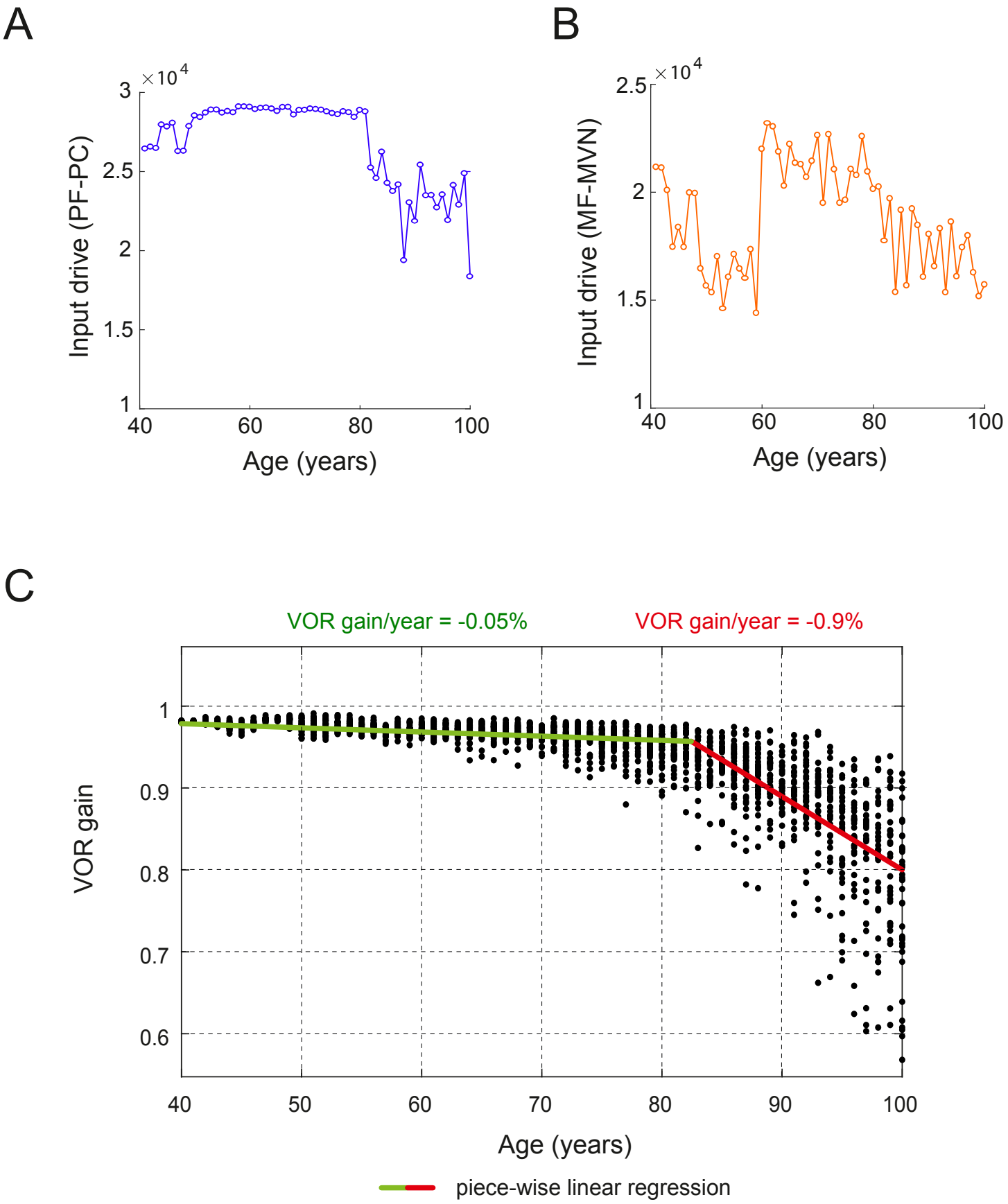

Figure 6

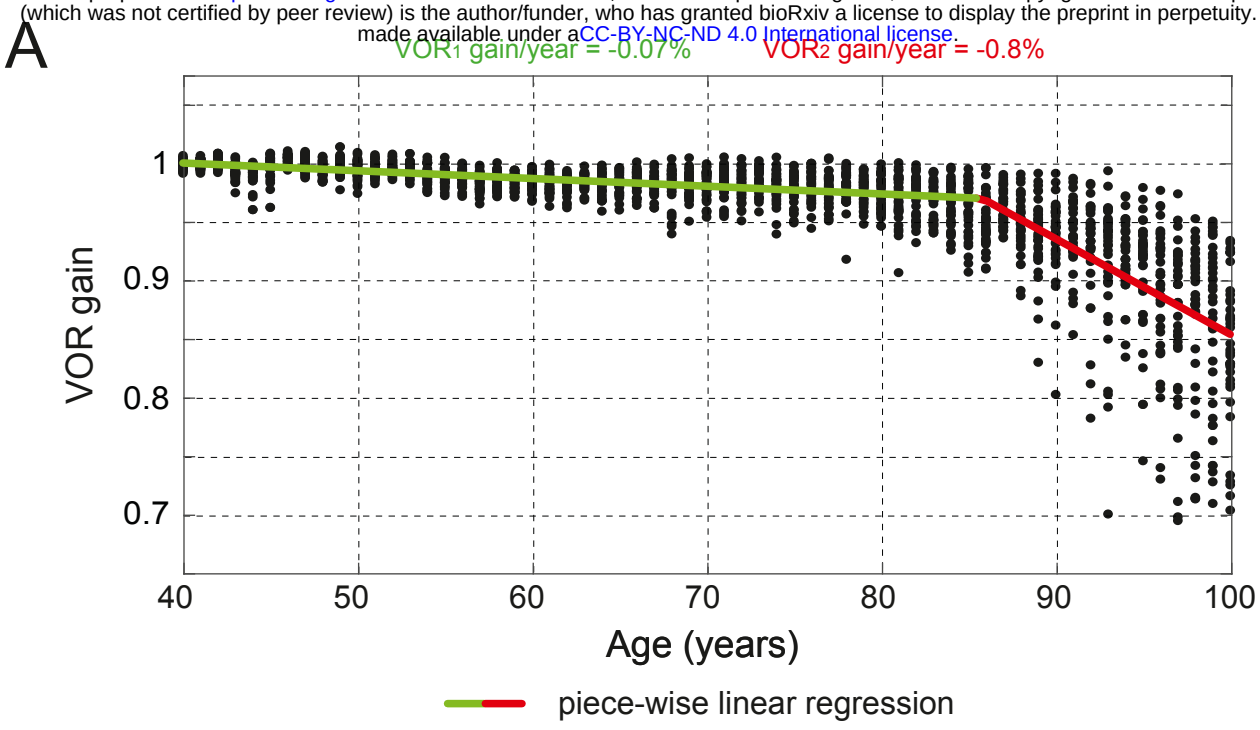

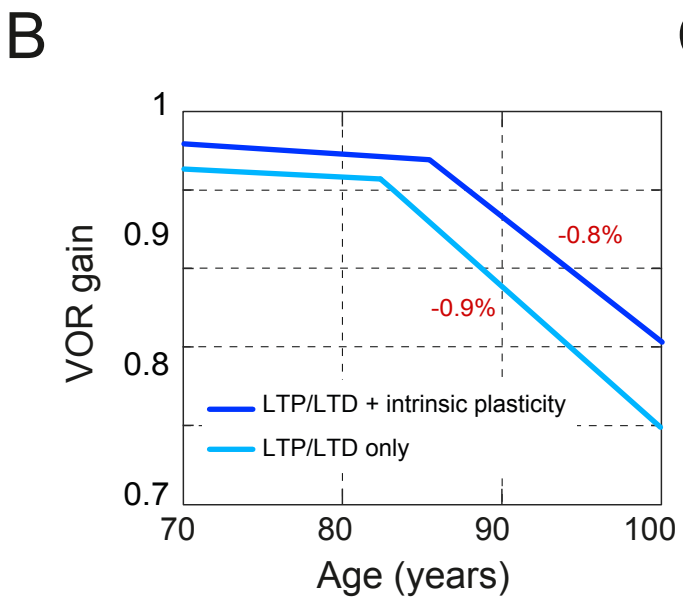

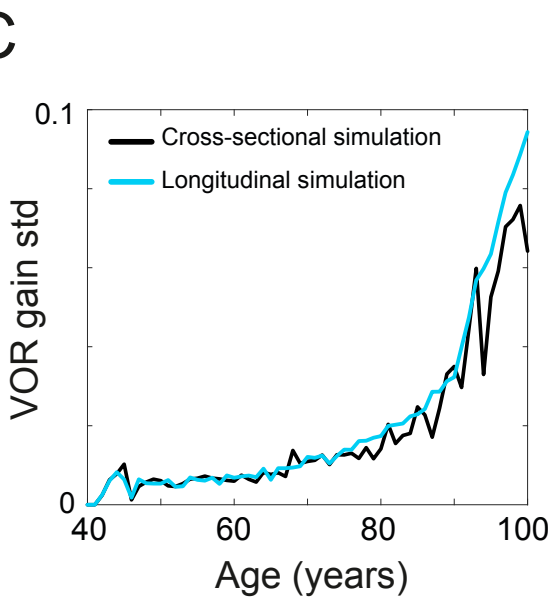

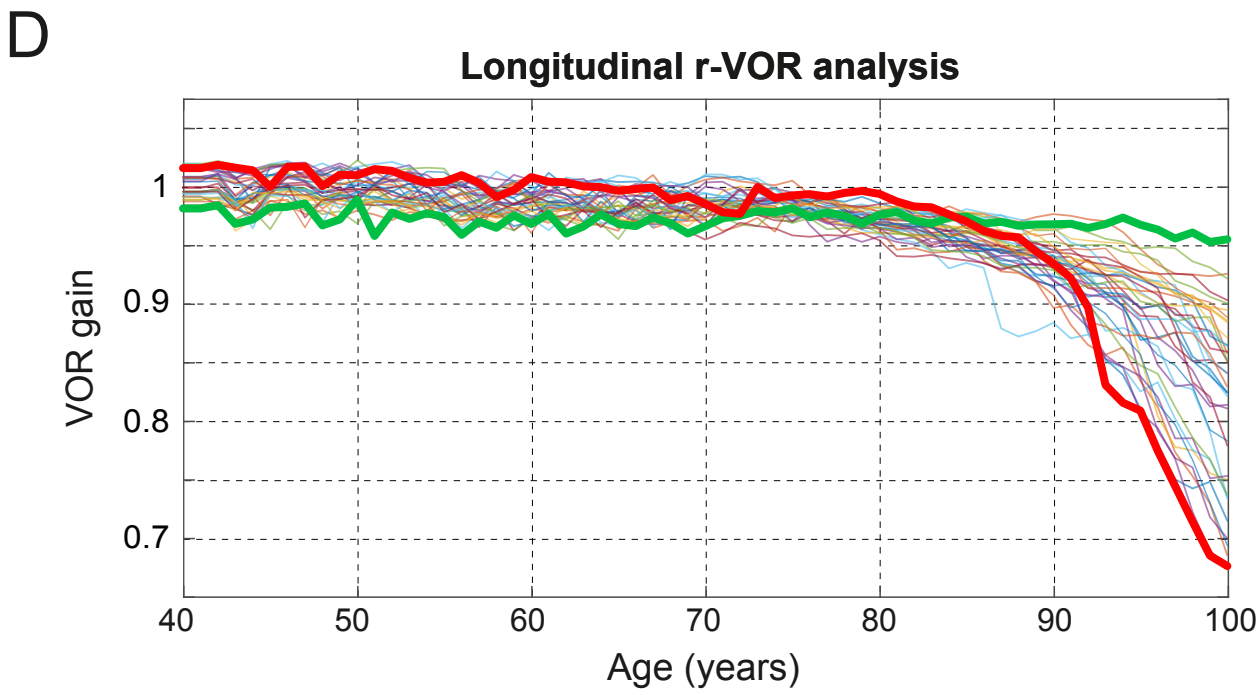

Figure 7

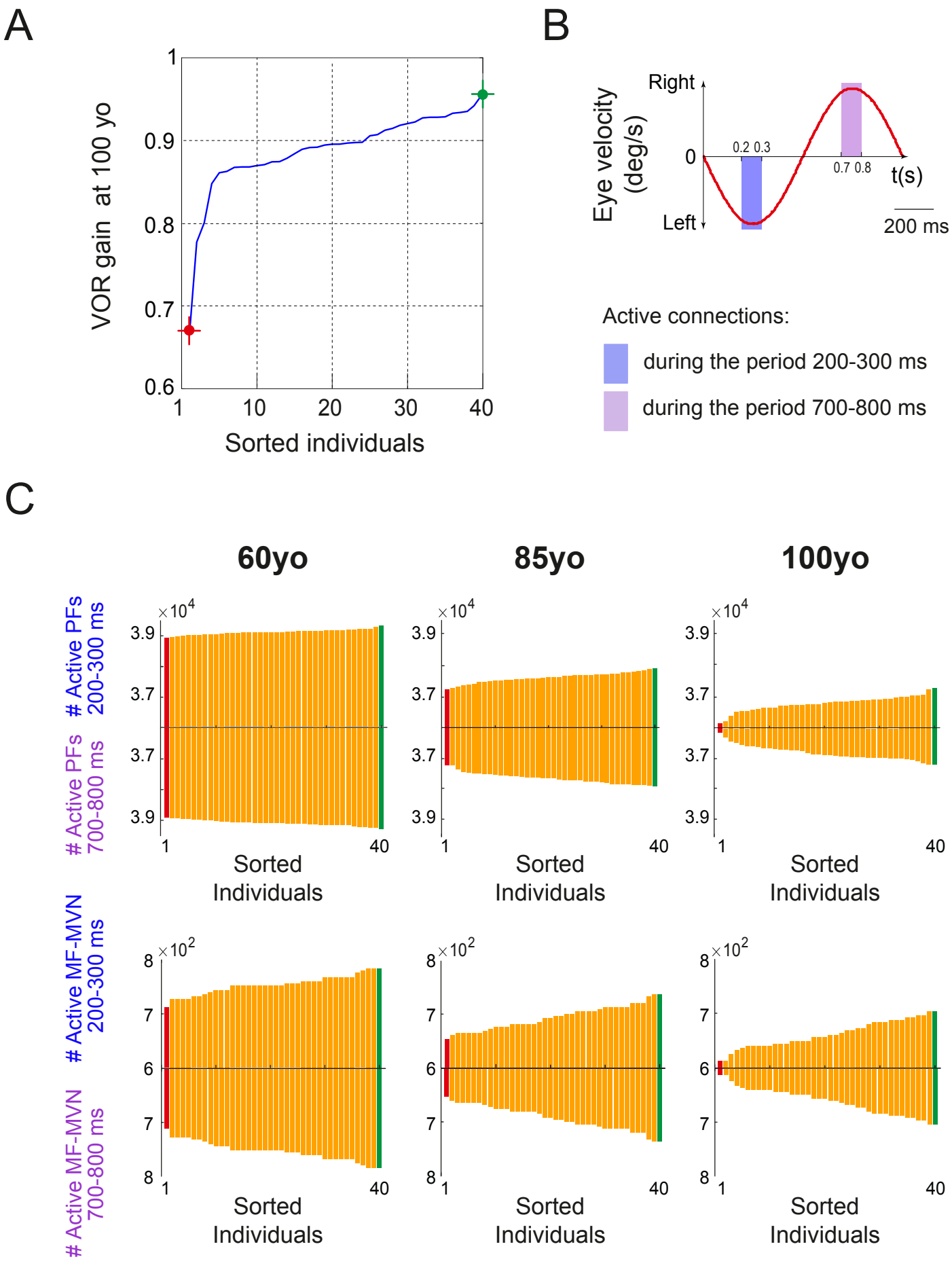

Figure 8

A

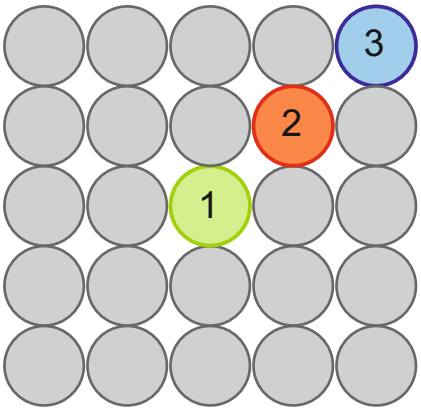

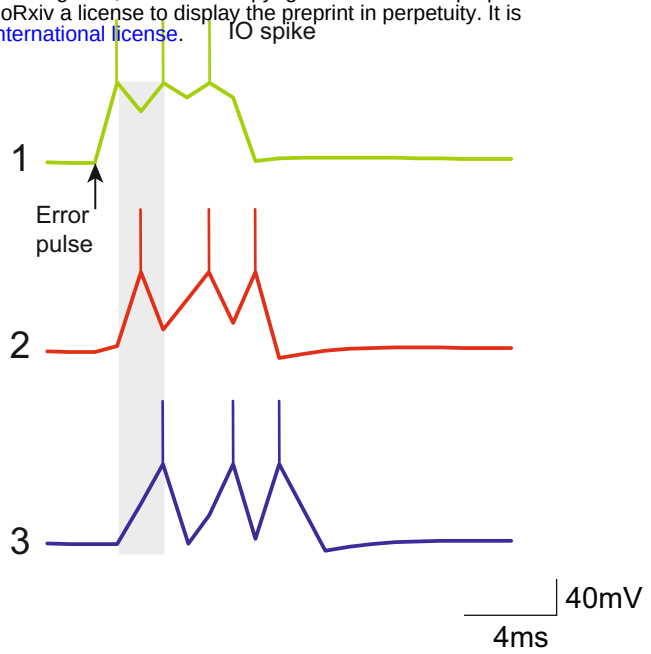

B

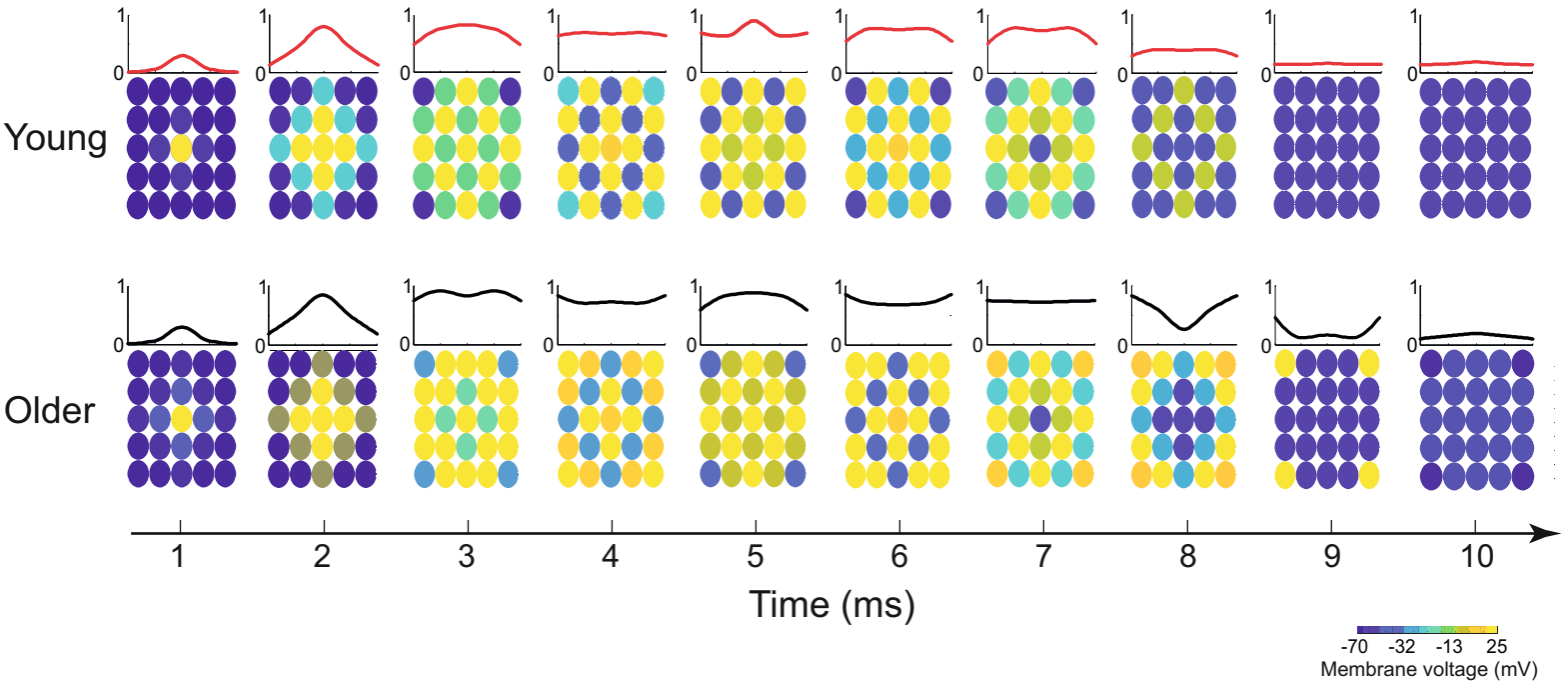

C

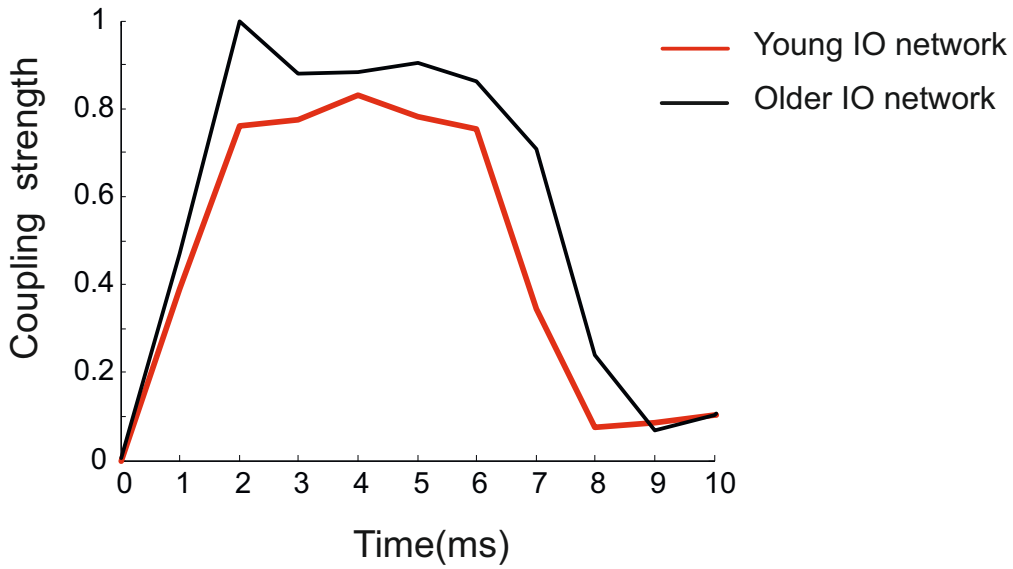

Supplementary Figure 1

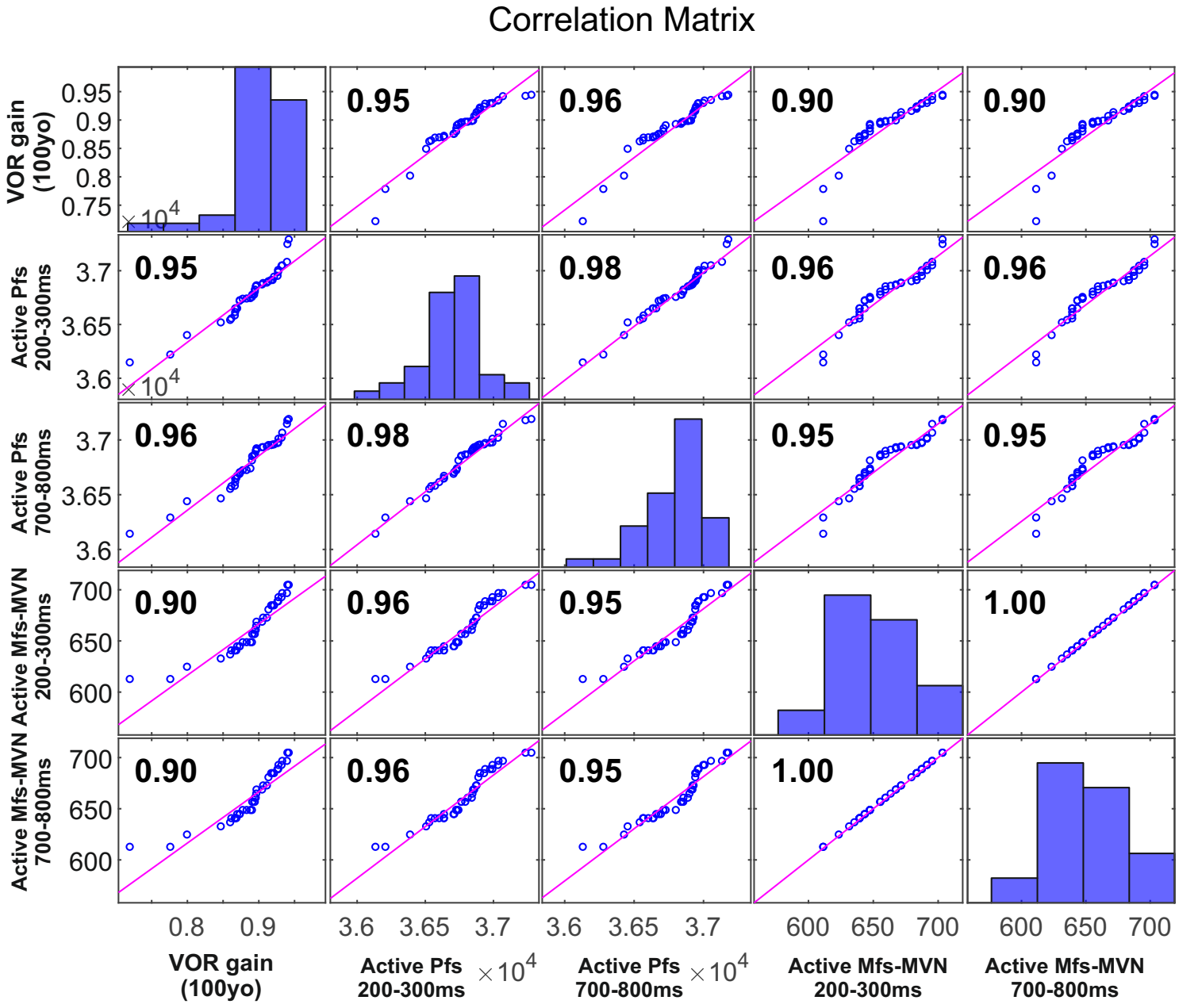

Figure S2